THE ASTROPHYSICAL JOURNAL, 466:191–223, 1996 July 20

RADIO RECOMBINATION LINES FROM INNER GALAXY DIFFUSE GAS. II. THE EXTENDED LOW-DENSITY WARM IONIZED MEDIUM AND THE "WORM-IONIZED MEDIUM"

CARL HEILES,[1] WILLIAM T. REACH,[2] AND BON-CHUL KOO[3]
Received 1995 July 17; accepted 1996 February 5

ABSTRACT

We have searched for 1.4 GHz radio recombination lines (RRLs) at 583 positions, mostly toward the galactic interior, and achieved detections at 418 positions. These data characterize the extended low-density warm ionized medium (the ELDWIM). We derive an electron temperature of 7000 K from a comparison of RRL and radio continuum, and estimate that non-LTE effects increase the line intensities by a factor of $\sim$1.3. We examine the distribution of the ELDWIM with a velocity-longitude diagram and find some concentration into spiral arms. The ELDWIM is not particularly well correlated with strong H II regions. The azimuthally symmetric inner Galaxy ring component of Taylor & Cordes does not appear in RRL emission, and we propose a revised model in which its electrons are located farther out in spiral arms. We derive the ELDWIM filling factor $\phi_{\rm WIM} \sim 0.01$ and an electron density in the emitting regions of ~ 5 cm^{-3}.

A fraction of the diffuse radio continuum and 100 μm IR emission is characterized by vertical structures that correspond well to the "worm" and "chimney" models, in which clustered supernovae blow large cavities in the gaseous disk that, for chimneys, connect to the gaseous halo. We interpret the RRL emission from these structures in terms of the "worm-ionized medium" (W-IM), in which the thermal radio emission arises in the worm walls; the walls are ionized by photons from hot stars in the cluster whose supernovae originally produced the cavity. The nearest example of a worm is the Orion/Eridanus cavity. The previously best-studied example is the Stockert chimney, which we argue is part of a much larger structure. The worms that have well-defined distances are closely confined to spiral arms. We discuss ionization requirements for worms and their associated H II regions and define three classes that describe the ionization of worm walls. These classes depend on the state of star formation in the central molecular cloud, which eventually dissipates. The global ionization requirement for all worm walls is small ($\sim$20%) compared to the total requirement for the Galactic ELDWIM. High-$|z|$ CO may be associated with at least two worms.

Subject headings: diffuse radiation — H II regions — ISM: bubbles — ISM: structure — radiative transfer — radio continuum: ISM — radio lines: ISM

1. INTRODUCTION

The warm ionized medium (WIM) is one of the four major components of the diffuse interstellar medium (Kulkarni & Heiles 1987). It amounts to $\sim$25% of the H I mass in the solar neighborhood. In the Galactic interior, $\langle n_e^2 \rangle$ becomes large enough for the WIM to become observable as the emitter of "diffuse recombination lines" (diffuse RRLs) at radio frequencies $\sim$1.4 GHz. The WIM in the Galactic interior was first considered by Mezger (1978), who called it the "extended low-density" (ELD) ionized gas. Here, following Petuchowski & Bennett (1993) and Heiles (1994), we refer to this gas as ELDWIM.

For several years we have been engaged in a survey of the inner Galaxy RRL emission from the ELDWIM at several hundred positions. The present paper discusses the primary goal of this survey, which was to map the RRL emission from "worm" structures[4] (Koo, Heiles, & Reach 1992). A portion of the ELDWIM resides in these worm structures; we denote such gas the "worm-ionized medium" (W-IM). The secondary goal of our survey was to determine the He^+/H^+ ratio, which is very small and is discussed in Paper I (Heiles et al. 1995, hereafter HKLR).

We discuss the observations in § 2. Section 3 compares RRL and continuum intensities to derive an approximate electron temperature. Section 4 discusses the location of the ELDWIM, argues that the Galactic electrons are concentrated into spiral arms (contrary to inferences from pulsar observations), presents a working model for the electron distribution, and then uses the model to derive the clumping factor and electron density of the ELDWIM. Section 5 presents a catalog of worms seen in thermal radio emission and discusses their sizes and ionization requirements. Section 6 discusses our results in terms of the worm/chimney paradigm. We summarize the main points in § 7.

2. OBSERVATIONS

2.1. *Data from Hat Creek Radio Observatory (HCRO)*

Some years ago we began the RRL survey with the 85 foot (26 m) telescope of HCRO, which no longer exists because it was destroyed by a windstorm on 1993 January 21. We observed many positions. Of the 583 positions in

[1] Astronomy Department, University of California at Berkeley, Berkeley, CA 94720.
[2] Universities Space Research Association, NASA/Goddard Space Flight Center, Code 685, Greenbelt, MD 20771.
[3] Seoul National University, Astronomy Department, Seoul 151-742, Korea.

[4] These structures are often referred to as "chimneys." In § 6 we discuss the difference between worms and chimneys, which boils down to the term "worm" being an observationally defined structure, while "chimney" is a theoretical construct. For convenience in nomenclature, we refer to all such objects as "worms."

Table 1, 443 were observed at HCRO; we detected the line in 305 of these positions. This telescope had HPBW = 36′ and was equipped with two ~40 K receivers in orthogonal circular polarizations and a 1024 channel spectral autocorrelator; details are in Heiles (1989). We established the calibration for brightness temperature by observing standard regions for the 21 cm line (Williams 1973). We observed RRLs at two frequencies and in two polarizations simultaneously. Most observations herein used the H165α and H167α RRLs, which are centered near 1451 and 1400 MHz, respectively; these RRLs were selected because they were quite clear of interference. A small fraction of observations used the H157α and H158α RRLs, which are centered near 1683 and 1651 MHz, respectively; these lines were prone to interference. In each case we observed a bandwidth of 5.0 MHz, frequency switched by 2.5 MHz, keeping the lines "within the band." With this arrangement, our total useful bandwidth is 2.5 MHz, which is equivalent to about 530 km s^{-1}, and the frequency resolution is 23.6 kHz (1.21 times larger than the channel separation; Cooper 1976), which is equivalent to about 5.0 km s^{-1}. We restricted our survey to positions having $|b| \geq 0.^{\circ}6$ because $b = 0°$ has already been surveyed by Lockman (1976, 1980) and Cersosimo (1990a, b). We detected the H RRL at many positions.

2.2. *Data from the National Radio Astronomy Observatory*[5]

After the demise of the HCRO telescope, we continued our survey with the 140 foot (43 m) telescope of NRAO. Of the 583 positions in Table 1, 144 were observed at NRAO; we detected the line in 113 of these positions. The larger fraction of detections at NRAO compared to HCRO occurs because the NRAO positions were selected either by using the results of the HCRO survey as a guide or to confirm marginal HCRO detections. This telescope has HPBW = 21′ and was equipped with two ~25 K receivers in orthogonal linear polarizations and a 1024 channel spectral autocorrelator. The autocorrelator specifications were the same as at Hat Creek, and we used the identical observing technique. We used different RRL transitions, depending on the interference environment; these included H165α (~1450 MHz), H168α (~1375 MHz), and H169α (~1350 MHz). We also tried the H166α line (~1425 MHz), but found the data to be unusable because of leakage of the much stronger 21 cm line into the image of the baseband mixer. The H168α RRL had little interference, but interference for the other transitions was more of a problem at NRAO than at HCRO and often allowed us to use only the H168α transition.

2.3. *Gaussian Fits and Estimates of Integrated Line Intensity*

We chose positions to observe from the "source component" of the 11 cm survey of Reich et al. (1990, hereafter RFRR). The RFRR source component is the total observed brightness temperature T_B minus the "diffuse component," which is a smoothed version (1° × 0.°3 in l and b) of T_B. The RFRR diffuse component is presented in their Figures 53–57 and is almost always brighter than the more structured source component. Where the RFRR source component is zero, we detect no RRL emission (§ 3 below); this is consistent with the expectation that the RFRR diffuse component is mostly large-scale Galactic synchrotron emission.

Table 1 lists all of the observed positions together with the Gaussian parameters of the RRL. Columns (1) and (2) are the Galactic coordinates. Column (3) is the intensity (brightness temperature in millikelvins); an entry in parentheses is an upper limit for a typical line width ~30 km s^{-1}, with no detection. Columns (4) and (5) are the velocity FWHM and the LSR velocity, both in kolometers per second. The final column contains comments, which are defined at the end of the table. "W" means a detection with low signal-to-noise ratio (discussed below). "GB" means the position was observed at NRAO and "HC" at HCRO, and an asterisk means that the position was observed at both; this occurred for eight positions, and we list both results. A comment such as S37 means that the position is close to the H II region of that number in the catalog by Sharpless (1959); however, a few associations may have inadvertently been missed.

Some of the spectra have more than one velocity component as noted (e.g., "2c" means "two components"). Figure 2 shows a selection of some less intense (but not necessarily classified as "W") two-component detections. In most cases these are multiple components of the H RRL, but some are He RRLs (the velocity displacement of He with respect to H is about −122 km s^{-1}). Some may be C RRLs (the velocity displacement of C with respect to H is about −150 km s^{-1}): non–H II region positions that might exhibit C RRLs include $(l, b) = (0.^{\circ}00, -0.^{\circ}60)$, $(16.^{\circ}40, 0.^{\circ}63)$, $(35.^{\circ}10, -1.^{\circ}50)$, $(81.^{\circ}00, -0.^{\circ}60)$. C RRLs are produced in photodissociation regions (HKLR). Some of the possible C RRLs are remarkably strong, and because of their possible interest we show a selection of the stronger ones in Figures 2*b* and 2*c*. Some of the possible C RRLs are on the brink of being "W's" and should be confirmed by further measurements.

2.4. *The Reality of our Detections*

We have carefully inspected our data, and we regard all detections listed in Table 1 as real. For the HCRO data our inspection process involved examining the two simultaneously observed RRL transitions with the following three steps. For the NRAO data, we often could rely only on the H168α transition because of interference, so we could not always follow the three steps.

1. Observe the position for the standard integration time of 1 hr using four simultaneous independent spectra: the RRL at two frequencies and two circular polarizations. This "standard integration time" varied by a factor of 2, either by accident or because some data were ruined by interference.

2. If the RRL was detected independently in all four spectra, we accepted the result as a detection and derived its parameters from the average of all four spectra. If there was no detection in all four spectra and, in addition, no detection in the average of all four spectra, we classified the results as a nondetection. Intermediate cases, in which the line appeared to be detected in only some of the spectra, were reobserved to provide additional integration time.

3. We examined the average of all data from step 2 and applied the same criterion, namely, if the line was detected in all four spectra, we accepted the result as real. If there was again an intermediate case we would usually obtain more

[5] The National Radio Astronomy Observatory (NRAO) is operated by Associated Universities, Inc., under contract with the National Science Foundation.

TABLE 1

POSITIONS OBSERVED AND GAUSSIAN FITS

l (1)	b (2)	T_b (3)	FWHM (4)	V_{LSR} (5)	Comments (6)
0.00	0.60	142.0	21.9	3.0	HC
0.00	−0.60	23.0	27.2	−141.5	HC; 2c
0.00	−0.60	173.0	31.8	12.1	HC; 2c
0.04	−1.32	13.0	42.1	5.3	HC
0.60	0.60	33.0	28.6	3.3	HC
0.60	−0.60	171.0	26.9	15.3	HC
1.19	−0.60	18.0	41.9	10.1	HC
1.20	0.60	13.0	32.7	8.5	HC
1.80	0.60	(8)	0.0	0.0	HC
1.80	−0.60	16.0	39.2	1.1	HC; W
2.00	3.40	(6)	0.0	0.0	HC
2.30	−1.10	6.1	34.9	2.8	GB
2.32	1.35	11.0	39.2	18.3	GB
2.40	0.60	14.0	29.4	15.3	HC
2.40	−0.60	(6)	0.0	0.0	HC
2.50	−1.60	(6)	0.0	0.0	HC
3.00	0.60	(6)	0.0	0.0	HC
3.00	3.40	(4)	0.0	0.0	GB*
3.00	3.40	(10)	0.0	0.0	HC*
3.00	−0.60	18.0	27.3	1.6	HC
3.10	−2.60	(2)	0.0	0.0	GB
3.30	−2.80	(6)	0.0	0.0	HC
3.60	0.60	15.0	16.6	6.9	HC
3.60	−0.60	21.0	28.3	5.2	HC
4.00	1.80	6.0	43.5	16.6	HC
4.10	−3.55	(4)	0.0	0.0	HC
4.20	0.60	22.0	28.9	9.2	HC
4.20	−0.60	17.0	32.1	13.9	HC
4.30	1.20	(4)	0.0	0.0	GB
4.40	1.70	12.0	19.0	12.5	HC
4.80	−0.60	25.0	28.2	8.9	HC
5.20	−1.60	10.0	29.0	6.6	HC
5.20	−2.60	(4)	0.0	0.0	HC
5.40	0.60	22.0	29.8	11.3	HC
5.40	−0.60	34.0	26.1	11.8	HC
5.48	0.02	52.7	27.0	13.7	GB
5.48	−0.25	42.1	23.3	14.1	GB
5.48	−0.58	40.4	22.9	16.5	GB
5.60	−2.10	(4)	0.0	0.0	HC
5.60	−3.40	(4)	0.0	0.0	HC
5.97	−1.18	252.0	24.9	1.7	HC
6.00	0.60	19.0	32.9	10.4	HC
6.00	−0.60	133.0	27.4	14.5	HC
6.00	−1.50	230.1	28.2	5.7	HC
6.60	0.60	27.0	24.5	16.0	HC
6.60	−0.60	97.0	26.3	17.6	HC
6.90	−2.12	69.6	21.4	8.8	GB; S29
6.90	−3.00	(3)	0.0	0.0	HC
7.00	−3.00	9.2	36.9	8.5	HC
7.00	−4.00	(8)	0.0	0.0	HC
7.19	−0.60	58.0	28.4	15.4	HC
7.20	0.60	39.0	33.8	15.2	HC
7.30	1.90	9.6	17.0	21.0	GB
7.50	1.20	16.2	18.0	18.3	GB
7.80	0.60	33.0	29.9	20.7	HC
7.80	1.00	15.7	34.0	8.5	GB
7.80	−0.60	25.0	43.4	29.0	HC
8.40	0.60	32.0	19.6	23.0	HC
8.40	−0.60	47.0	34.4	29.0	HC
8.70	−4.90	(3)	0.0	0.0	GB*
8.70	−4.90	(5)	0.0	0.0	HC*
9.00	0.60	28.0	24.2	20.0	HC
9.00	−0.60	30.0	25.3	19.9	HC
9.60	0.60	21.0	43.2	22.9	HC
9.60	1.20	7.2	44.8	8.9	GB
9.60	−0.60	32.0	43.6	26.4	HC
10.20	0.60	11.0	42.5	30.2	HC
10.20	−0.60	85.0	39.6	15.9	HC
10.20	−1.20	31.0	31.2	25.1	HC
10.20	−1.80	(9)	0.0	0.0	HC
10.20	−2.40	9.6	44.9	21.4	GB

TABLE 1—*Continued*

l (1)	b (2)	T_b (3)	FWHM (4)	V_{LSR} (5)	Comments (6)
10.20	−3.00	8.5	36.8	26.7	GB
10.20	−3.60	(3)	0.0	0.0	GB
10.20	−4.10	9.3	29.9	19.1	GB
10.20	−4.80	(5)	0.0	0.0	GB
10.30	4.40	(4)	0.0	0.0	HC
10.30	−3.00	(4)	0.0	0.0	HC
10.50	−1.40	23.0	36.5	24.7	HC
10.70	−2.20	10.0	38.7	10.0	HC; W
10.80	0.60	21.0	46.1	35.3	HC
10.80	−0.60	47.0	46.7	10.9	HC
10.80	−2.40	15.7	42.7	22.3	GB
10.80	−3.00	5.1	26.2	30.8	GB
10.80	−4.80	(4)	0.0	0.0	GB
10.90	−1.90	28.0	34.8	18.0	HC
11.00	1.10	16.2	54.1	22.5	GB
11.10	1.65	4.3	33.5	59.5	GB
11.10	1.65	6.0	30.6	16.2	GB
11.15	1.15	9.4	40.3	28.0	GB
11.20	−1.10	27.0	29.9	18.4	HC
11.25	2.05	4.5	66.3	14.1	GB
11.40	0.60	30.0	39.5	33.1	HC
11.40	−0.60	29.0	37.7	28.0	HC
11.60	−3.50	(5)	0.0	0.0	GB
11.60	−3.50	(5)	0.0	0.0	HC
11.65	−1.72	21.0	30.9	12.2	HC; S37
11.80	−2.40	7.1	65.7	15.4	GB
12.00	0.60	32.0	38.1	31.8	HC
12.00	−0.60	41.0	37.9	37.0	HC
12.10	1.60	17.0	36.3	35.1	HC
12.30	1.30	25.0	32.9	31.4	HC
12.45	−1.12	19.0	41.1	27.7	HC; S39
12.60	0.60	31.0	36.6	29.2	HC
12.60	−0.60	71.0	36.3	32.9	HC
12.90	0.70	27.8	35.5	38.3	GB
13.20	0.60	31.0	33.6	30.1	HC
13.20	−0.60	38.0	46.3	30.2	HC
13.25	1.70	13.6	29.9	24.4	GB
13.41	1.46	7.8	51.4	81.2	GB; near S42; 2c; W
13.41	1.46	18.0	36.5	19.9	GB; near S42; 2c
13.80	0.60	28.0	34.5	27.7	HC
13.80	−0.60	62.0	32.7	28.7	HC
13.80	−1.20	25.0	25.0	20.7	HC
13.80	−1.80	12.0	28.8	19.5	HC
13.80	−2.40	6.0	41.3	27.1	HC; W
14.05	1.25	14.8	40.9	25.9	GB
14.40	0.60	42.0	32.6	27.2	HC
14.40	−0.60	80.0	36.2	26.5	HC
14.40	−1.20	21.0	49.1	29.9	HC
14.40	−1.80	11.0	71.1	28.2	HC
14.40	−2.40	7.9	18.4	22.6	GB
14.60	−1.63	15.8	32.2	21.0	GB
15.00	0.60	30.0	36.8	28.6	HC
15.00	−0.60	65.0	26.8	−131.2	HC; near S45
15.00	−0.60	478.0	37.5	18.8	HC; near S45
15.00	−1.20	9.5	84.9	−84.9	GB; 2c
15.00	−1.20	65.0	46.5	22.2	GB; 2c
15.00	−1.63	32.7	29.8	23.9	GB
15.00	−1.80	19.0	28.7	28.3	HC
15.00	−2.40	7.0	36.8	32.6	HC; W
15.05	−0.68	147.6	27.1	−103.3	GB; M17; 4c; note 1
15.05	−0.68	203.6	18.5	−133.8	GB; M17; 4c; note 1
15.05	−0.68	250.2	78.2	17.6	GB; M17; 4c; note 1
15.05	−0.68	1287.0	37.2	18.6	GB; M17; 4c; note 1
15.10	3.25	38.1	19.6	19.7	GB; S46
15.13	3.33	32.6	21.6	19.2	GB
15.13	−3.33	(6)	0.0	0.0	HC
15.30	4.00	(9)	0.0	0.0	HC
15.60	0.60	27.0	40.4	27.6	HC
15.60	1.20	20.0	27.5	26.8	HC
15.60	1.80	16.0	27.0	25.1	HC
15.60	−0.60	87.0	38.3	23.3	HC
15.60	−1.20	25.0	38.4	28.2	HC

TABLE 1—*Continued*

l (1)	b (2)	T_b (3)	FWHM (4)	V_{LSR} (5)	Comments (6)
15.60	−1.80	20.0	18.2	31.4	HC
15.60	−2.40	18.6	23.1	33.3	GB
15.70	−2.00	18.0	28.6	37.6	HC; W
15.80	0.63	31.0	29.4	28.3	HC
15.90	−1.90	19.9	42.8	31.1	GB
16.10	2.30	13.0	37.2	25.9	HC
16.20	0.60	36.0	40.1	17.9	HC
16.20	1.20	23.0	31.7	23.5	HC
16.20	1.80	13.0	36.0	30.3	HC
16.20	−0.60	36.0	34.1	36.1	HC
16.20	−1.20	11.0	60.5	41.5	HC
16.20	−1.80	8.0	37.9	31.5	HC; W
16.20	−2.40	20.0	19.1	28.8	HC
16.30	−3.10	11.0	19.9	32.6	HC; W
16.40	0.63	21.7	22.1	−134.3	HC; 2c
16.40	0.63	67.8	27.3	25.3	HC; 2c
16.46	1.28	53.0	37.9	24.6	HC
16.50	3.00	(4)	0.0	0.0	GB
16.60	0.60	93.0	28.4	24.3	HC
16.60	1.20	57.0	27.9	25.1	HC
16.80	0.60	182.0	26.7	22.0	HC; S49
16.80	1.80	22.0	36.3	21.9	HC
16.80	−0.60	36.0	40.8	36.3	HC
16.90	−2.40	18.0	26.4	23.6	HC
17.00	0.63	266.0	28.7	24.3	HC
17.06	1.28	115.0	25.0	24.9	HC
17.10	−3.10	11.8	28.6	29.5	GB
17.40	0.60	138.0	24.2	21.7	HC
17.40	1.20	98.0	22.3	23.4	HC
17.40	1.80	30.0	35.7	24.1	HC
17.40	2.40	18.0	22.2	26.0	HC
17.40	3.00	6.3	45.8	21.0	GB
17.40	−0.60	22.0	49.0	39.0	HC
17.40	−2.40	10.3	44.6	29.2	GB
17.66	1.28	54.0	26.4	22.5	HC
17.80	−2.70	(5)	0.0	0.0	GB
18.00	0.60	35.0	28.3	21.9	HC
18.00	1.20	57.0	29.5	25.8	HC
18.00	1.80	109.0	22.0	26.0	HC
18.00	2.40	86.0	21.1	27.9	HC
18.00	3.00	17.0	32.6	33.3	GB
18.00	−0.60	36.0	25.6	47.2	HC
18.00	−1.20	14.0	51.7	41.8	HC
18.00	−1.80	9.1	45.5	45.5	GB
18.05	0.83	34.0	23.1	21.2	HC
18.25	2.70	53.1	23.6	26.9	GB; note 1
18.47	1.93	329.0	27.0	30.5	GB; S54; note 1
18.60	0.60	21.0	55.9	45.8	HC
18.60	1.20	61.0	27.0	28.9	HC
18.60	1.80	316.3	27.4	30.4	near S54
18.60	2.40	101.0	27.5	27.9	GB; note 1
18.60	3.00	37.6	22.1	26.5	GB
18.60	3.60	32.0	21.3	24.7	HC
18.60	4.20	10.2	16.2	23.5	GB
18.60	4.80	(4)	0.0	0.0	HC
18.60	6.00	(9)	0.0	0.0	HC
18.60	−0.60	63.0	36.1	58.3	HC
18.60	−1.20	15.0	47.5	55.0	HC
18.60	−1.80	6.8	54.2	41.1	HC
18.65	0.83	20.0	51.0	41.2	HC
18.75	2.00	202.1	30.8	28.7	HC
19.20	0.60	29.0	38.0	43.5	HC
19.20	1.20	33.0	33.9	30.0	HC
19.20	1.80	69.0	25.6	26.2	HC
19.20	2.40	31.0	30.7	24.8	HC
19.20	3.00	12.2	33.3	24.6	GB
19.20	3.20	11.0	28.3	28.5	HC
19.20	−0.60	93.0	29.4	59.4	HC
19.20	−1.20	17.0	41.1	49.7	HC
19.20	−1.80	10.0	60.2	55.0	HC
19.25	0.83	27.0	37.3	41.0	HC
19.80	0.60	17.0	44.7	37.2	HC

TABLE 1—*Continued*

l (1)	b (2)	T_b (3)	FWHM (4)	V_{LSR} (5)	Comments (6)
19.80	1.20	19.0	28.9	29.6	HC
19.80	1.80	14.0	34.8	23.3	HC
19.80	2.40	24.0	15.2	21.3	HC
19.80	3.00	7.9	44.6	23.7	GB
19.80	−0.60	33.0	34.3	51.2	HC
19.80	−1.20	21.0	41.3	48.7	HC
19.80	−1.80	9.0	83.8	47.0	HC
20.40	0.60	15.0	31.4	27.5	HC
20.40	1.20	12.0	33.9	22.6	HC
20.40	1.80	5.5	55.4	38.0	GB
20.40	−0.60	26.0	30.1	59.1	HC
20.40	−1.20	16.0	46.5	52.6	HC; S55
20.40	−1.80	(6)	0.0	0.0	HC
20.60	3.00	6.1	27.7	29.4	GB
21.00	0.60	11.0	67.9	79.0	HC
21.00	1.20	16.0	22.5	36.5	HC
21.00	1.80	11.7	16.9	28.8	GB
21.00	−0.60	21.0	73.4	55.3	HC
21.12	1.40	20.0	16.2	31.1	HC
21.60	−1.20	(6)	0.0	0.0	HC
21.60	−1.80	(6)	0.0	0.0	HC
22.20	−0.60	44.0	34.6	77.9	HC
22.20	−1.20	15.0	37.9	77.3	HC
22.20	−1.80	(6)	0.0	0.0	HC
22.40	3.75	(3)	0.0	0.0	HC
22.80	−0.60	98.0	29.2	74.3	HC
22.80	−1.20	18.0	38.7	78.5	HC
22.80	−1.80	(3)	0.0	0.0	GB
23.30	−1.50	3.6	72.8	75.8	GB; W
23.40	−0.60	64.0	46.8	75.3	HC
23.40	−1.20	9.5	46.9	72.5	GB
23.40	−1.80	(11)	0.0	0.0	HC
23.40	−3.40	9.0	12.8	86.6	HC; W
24.00	−1.20	12.9	38.6	52.7	GB; 2c
24.00	−1.20	13.4	32.5	105.0	GB; 2c
24.00	−1.80	(4)	0.0	0.0	GB
24.60	−0.60	35.8	44.7	105.3	GB; 2c
24.60	−0.60	47.4	24.5	49.0	GB; 2c
25.20	−0.60	37.0	67.8	85.4	HC
25.20	−1.80	(9)	0.0	0.0	HC
25.20	−2.30	(3)	0.0	0.0	GB
25.40	1.70	16.0	13.3	43.5	HC; W
25.40	−2.40	(5)	0.0	0.0	GB
25.60	1.40	17.3	23.7	42.9	GB
25.70	0.90	24.0	19.3	101.3	HC
25.70	0.90	27.0	12.6	39.2	HC
25.80	2.10	(4)	0.0	0.0	HC
25.80	−2.40	(4)	0.0	0.0	GB
26.20	2.70	(9)	0.0	0.0	HC
26.25	−2.95	(2)	0.0	0.0	GB
26.35	−3.37	(2)	0.0	0.0	GB
26.37	1.43	5.6	31.7	96.2	GB; near S61; 2c
26.37	1.43	11.7	26.5	47.0	GB; near S61; 2c
26.40	−3.00	(10)	0.0	0.0	HC
26.75	1.20	8.2	42.0	94.8	GB; 2c
26.75	1.20	10.8	23.2	41.8	GB; 2c
27.00	−0.60	35.0	56.9	86.0	HC
27.40	−2.06	(4)	0.0	0.0	HC
27.60	−0.60	33.0	34.1	92.9	HC
27.60	−2.40	(5)	0.0	0.0	HC
28.20	2.40	(9)	0.0	0.0	HC
28.20	−0.60	22.1	35.6	84.7	GB
28.20	−2.40	(5)	0.0	0.0	HC
28.25	−0.50	12.2	48.3	34.1	HC; 2c
28.25	−0.50	42.6	43.8	90.7	HC; 2c
28.40	−2.10	(3)	0.0	0.0	HC
28.50	−1.00	8.9	35.2	32.5	HC; 2c
28.50	−1.00	18.6	66.4	87.4	HC; 2c
28.80	3.00	10.0	22.5	2.9	HC
28.80	3.60	52.0	27.5	1.2	HC; S64
29.08	2.76	(4)	0.0	0.0	HC
29.25	−0.50	35.7	32.7	51.0	HC; S65; 2c

TABLE 1—*Continued*

l (1)	b (2)	T_b (3)	FWHM (4)	V_{LSR} (5)	Comments (6)
29.25	−0.50	59.3	41.4	96.1	HC; S65; 2c
29.40	1.20	10.0	34.4	83.2	HC
29.50	−1.00	9.0	30.4	43.8	HC; 2c; W
29.50	−1.00	21.4	47.0	90.6	HC; 2c
29.60	1.40	6.0	63.4	98.9	GB
29.70	1.35	(3)	0.0	0.0	GB
29.75	−1.50	12.4	41.8	91.4	HC
30.00	0.00	213.0	33.0	100.0	HC
30.00	1.20	(10)	0.0	0.0	HC
30.00	1.80	(9)	0.0	0.0	HC
30.00	2.40	(9)	0.0	0.0	HC
30.00	−0.60	96.0	23.6	96.7	HC
30.00	−2.00	6.1	73.4	82.3	HC
30.13	1.35	7.8	36.2	96.4	GB
30.25	−0.50	31.5	71.2	80.2	GB; 2c; note 1
30.25	−0.50	123.3	24.6	101.2	GB; 2c; note 1
30.50	1.35	4.2	59.7	91.6	GB
30.50	−1.00	39.9	56.9	90.2	HC
30.60	−0.60	102.0	36.3	96.4	HC
30.60	−2.10	(6)	0.0	0.0	HC
30.75	0.00	54.1	38.2	−63.5	HC; W43; 4c
30.75	0.00	55.9	15.8	−31.4	HC; W43; 4c
30.75	0.00	102.5	47.9	41.6	HC; W43; 4c
30.75	0.00	389.4	40.5	98.6	HC; W43; 4c
30.75	−1.50	16.1	80.2	88.4	HC
30.76	−0.03	38.9	18.8	−57.5	GB; W43; 4c; note 1
30.76	−0.03	21.0	18.0	−27.6	GB; W43; 4c; note 1
30.76	−0.03	97.0	26.5	45.4	GB; W43; 4c; note 1
30.76	−0.03	587.0	36.6	95.6	GB; W43; 4c; note 1
30.80	−1.40	14.0	49.3	93.3	GB
31.00	−2.00	8.0	78.0	96.2	HC
31.20	−0.60	48.0	42.0	96.7	HC
31.25	−0.50	103.0	37.7	96.6	HC
31.25	−2.50	5.0	83.0	97.9	HC
31.50	1.43	7.8	52.0	80.4	GB
31.50	−1.00	10.5	57.3	58.3	GB; 2c
31.50	−1.00	10.7	31.6	101.7	GB; 2c
31.50	−2.30	(4)	0.0	0.0	HC
31.50	−3.00	6.3	132.0	71.8	HC; note 2
31.75	−1.50	9.0	65.7	89.4	HC
31.90	1.43	20.2	27.0	55.1	GB; S69
32.00	−2.00	6.1	80.4	76.6	HC
32.25	−0.50	24.1	40.9	95.1	HC; 2c
32.25	−0.50	25.5	46.2	41.0	HC; 2c
32.30	1.43	6.5	70.0	79.8	GB
32.50	−1.00	5.5	55.2	27.2	HC; 2c; W
32.50	−1.00	9.4	88.6	97.3	HC; 2c
33.60	−0.60	14.0	63.7	73.4	HC
33.78	−0.90	8.2	42.0	57.5	GB
34.20	−0.60	75.0	6.2	54.1	HC
34.20	−1.80	(6)	0.0	0.0	HC
34.65	−1.50	12.7	28.1	60.0	GB; W
34.80	1.60	(5)	0.0	0.0	GB
34.80	−0.60	20.0	36.0	52.2	HC
34.80	−1.20	19.0	26.0	47.0	HC
34.80	−1.80	5.5	31.1	60.1	GB; W
34.90	1.48	9.7	57.1	73.5	GB
35.10	1.20	23.0	23.2	77.3	HC; W
35.10	−1.50	20.1	54.0	−126.6	GB; 2c
35.10	−1.50	46.4	21.3	42.4	GB; 2c
35.40	−0.60	47.0	27.8	56.0	HC
35.40	−1.20	(7)	0.0	0.0	HC
35.40	−1.80	17.0	37.1	48.2	HC
36.00	−0.60	25.0	40.6	61.0	HC
36.00	−1.20	(10)	0.0	0.0	HC
36.10	−2.20	(4)	0.0	0.0	GB
36.30	−1.67	50.7	20.9	63.1	GB*
36.30	−1.70	25.0	24.0	62.4	HC*; S72
36.60	−0.60	17.0	58.7	64.5	HC
36.60	−1.20	9.0	26.8	66.6	HC
37.20	−0.60	20.0	34.6	46.8	HC
37.30	1.00	30.3	20.9	44.6	GB

TABLE 1—*Continued*

l (1)	b (2)	T_b (3)	FWHM (4)	V_{LSR} (5)	Comments (6)
37.60	1.60	25.0	23.8	44.1	HC
37.60	2.10	13.1	20.3	42.1	GB
37.80	−0.60	38.0	38.9	59.4	HC
38.10	1.75	20.4	19.9	43.3	GB
38.30	1.20	28.0	15.9	36.7	HC
38.40	2.25	(5)	0.0	0.0	GB
38.70	2.70	(2)	0.0	0.0	GB
39.25	3.00	(4)	0.0	0.0	GB
39.50	−1.70	(6)	0.0	0.0	HC
39.60	−0.60	19.0	48.2	57.9	HC
39.90	−1.32	25.7	24.2	46.7	GB; S74
39.90	−2.10	(7)	0.0	0.0	HC
40.00	−3.20	(6)	0.0	0.0	HC
40.55	2.50	34.8	28.3	27.2	GB*; S76
40.60	2.50	19.0	26.3	30.6	HC*
40.90	2.75	3.4	44.9	37.5	GB
41.00	3.20	(4)	0.0	0.0	HC
41.30	−1.20	(2)	0.0	0.0	GB
41.90	−3.70	(3)	0.0	0.0	HC
43.17	0.00	48.6	28.8	58.7	GB; W49; 2c
43.17	0.00	165.6	29.1	8.4	GB; W49; 2c
43.20	−0.60	23.0	18.6	53.4	HC; W
43.50	0.50	(6)	0.0	0.0	HC
43.50	1.00	(9)	0.0	0.0	HC
43.50	1.50	9.0	33.0	31.7	HC; W
43.50	2.00	(6)	0.0	0.0	HC
43.80	1.20	(4)	0.0	0.0	HC
43.80	1.80	(4)	0.0	0.0	HC
43.90	1.20	(9)	0.0	0.0	HC
44.00	0.50	9.0	37.6	43.5	HC; W
44.00	1.00	8.0	128.0	43.5	HC
44.00	1.50	(9)	0.0	0.0	HC
44.00	2.00	(8)	0.0	0.0	HC
44.00	3.00	(7)	0.0	0.0	HC
44.50	0.50	8.0	35.4	41.9	HC; W
44.50	1.00	(6)	0.0	0.0	HC
44.50	1.50	5.0	40.1	40.5	HC; W
44.50	2.00	9.0	34.3	46.8	HC; W
45.00	−1.20	(8)	0.0	0.0	HC
45.20	−1.10	(4)	0.0	0.0	HC
45.60	0.60	(7)	0.0	0.0	HC
45.60	1.20	(6)	0.0	0.0	HC
46.00	−1.20	(4)	0.0	0.0	GB
46.20	0.60	(10)	0.0	0.0	HC
46.20	1.20	(9)	0.0	0.0	HC
46.20	−1.80	(6)	0.0	0.0	HC
46.80	0.60	(6)	0.0	0.0	HC
46.80	1.20	(8)	0.0	0.0	HC
48.00	−1.30	9.1	25.1	65.2	GB
48.10	−1.00	18.0	18.0	63.3	HC
48.50	−0.50	42.0	28.0	58.7	HC; near W51
48.50	−1.00	10.0	11.6	63.3	HC; near W51
49.00	−0.50	161.0	26.3	58.8	HC; near W51 (S79)
49.00	−1.00	15.0	27.4	53.5	HC; near W51
49.20	−0.60	164.0	29.7	58.2	HC
49.48	−0.38	376.1	34.4	58.5	GB
49.50	−0.50	149.0	31.6	56.3	HC; near W51
49.50	−1.00	12.9	32.5	67.1	GB
49.80	−1.20	5.1	43.1	65.5	GB
49.80	−1.80	(9)	0.0	0.0	HC
50.00	−0.50	18.0	30.9	56.8	HC; near W51
50.00	−1.00	(7)	0.0	0.0	HC
50.00	−1.54	(2)	0.0	0.0	GB*
50.00	−1.60	(4)	0.0	0.0	HC*
53.40	−1.20	(4)	0.0	0.0	GB
53.40	−1.40	(9)	0.0	0.0	HC
53.40	−2.40	(9)	0.0	0.0	HC
55.20	−0.60	9.3	23.7	32.4	GB
57.00	0.60	(7)	0.0	0.0	HC
57.00	1.20	9.0	30.5	36.2	HC
57.00	1.80	(6)	0.0	0.0	HC
57.00	2.40	(7)	0.0	0.0	HC

TABLE 1—*Continued*

l (1)	b (2)	T_b (3)	FWHM (4)	V_{LSR} (5)	Comments (6)
59.76	0.90	11.3	20.1	24.8	GB
61.45	0.28	15.0	28.1	23.8	HC
61.50	−0.94	9.0	21.0	27.0	HC
61.80	−0.60	11.2	23.6	23.0	GB
62.90	0.10	26.1	22.1	21.8	GB
63.00	0.00	18.0	21.8	21.7	HC
63.00	0.60	12.6	32.7	23.7	GB
63.00	1.20	(7)	0.0	0.0	HC
63.00	1.80	(6)	0.0	0.0	HC
63.00	2.40	(7)	0.0	0.0	HC
63.00	3.00	(7)	0.0	0.0	HC
63.00	−0.60	(6)	0.0	0.0	HC
63.00	−1.20	(7)	0.0	0.0	HC
63.00	−1.80	(6)	0.0	0.0	HC
63.00	−2.40	(6)	0.0	0.0	HC
63.00	−3.00	(6)	0.0	0.0	HC
63.35	−0.77	(5)	0.0	0.0	HC*
63.35	−0.77	(6)	0.0	0.0	GB*
63.65	−0.72	9.7	17.1	17.4	GB
64.08	1.58	13.0	47.2	23.7	HC; S92
68.16	1.00	11.0	20.2	1.8	HC; S98
69.00	2.50	(6)	0.0	0.0	HC
69.86	1.53	19.0	73.8	−39.4	GB
69.88	1.61	28.1	31.9	−23.6	GB; near S100
70.26	1.61	45.1	24.9	−25.2	GB*; S100
70.27	1.64	29.0	20.2	−27.9	HC*; S100
71.59	2.82	22.0	16.0	13.1	HC; S101
71.86	2.44	20.0	29.7	14.5	HC
72.08	2.79	18.0	26.0	9.5	HC
72.17	2.38	16.0	17.5	13.1	HC
72.24	−1.37	9.0	26.4	6.2	HC
73.65	−1.93	9.0	25.1	6.5	HC
74.48	−0.99	9.0	31.9	1.7	HC
74.76	4.54	(2)	0.0	0.0	GB
75.07	−1.68	8.0	32.4	7.7	HC
75.47	2.44	11.0	22.3	9.7	HC; S105
75.60	−0.60	16.8	48.6	4.3	GB*; S106
75.60	−0.75	12.0	30.9	2.4	HC*
75.82	0.38	32.0	32.3	−7.2	HC
76.00	2.00	15.0	23.9	10.6	HC
76.76	−1.18	24.3	27.8	3.7	GB
76.82	4.30	12.7	32.8	4.3	GB
77.00	2.00	37.0	32.2	4.1	HC
77.40	−0.60	32.0	14.6	0.4	HC
77.68	−2.26	15.9	29.5	3.3	GB
78.00	2.00	55.0	31.1	−1.4	HC
78.03	0.61	19.0	32.3	−6.2	HC
78.35	−1.17	46.0	35.2	−2.5	GB
79.00	2.00	28.0	22.6	5.5	HC; 2c
79.00	2.00	34.0	24.9	−26.9	HC; 2c
79.05	3.61	84.0	23.0	−3.6	HC
79.11	3.00	37.0	33.2	5.5	HC
79.20	−0.60	90.0	28.4	−1.1	HC
79.60	−1.42	52.0	19.3	0.0	HC
80.35	4.72	25.0	32.8	0.8	HC
80.93	−0.16	70.0	29.4	−3.2	HC
81.00	0.00	84.0	28.1	0.1	HC
81.00	−0.60	8.0	42.8	−147.6	HC; 2c; W
81.00	−0.60	41.0	24.1	−1.1	HC; 2c
81.00	−1.20	35.0	21.1	−2.0	HC
81.00	−1.80	23.0	18.0	−0.8	HC
81.00	−2.40	13.0	21.5	−0.6	HC
81.00	−3.00	8.3	30.2	−0.1	GB
81.00	−3.60	(6)	0.0	0.0	HC
81.00	−4.20	(7)	0.0	0.0	HC
81.00	−4.80	(6)	0.0	0.0	HC
81.38	−1.20	41.0	27.5	−2.8	HC
82.00	2.00	42.0	25.0	−5.6	HC
82.25	2.42	111.0	25.0	−4.7	HC
82.57	0.40	61.0	30.8	−4.6	HC
82.80	−0.60	44.0	36.7	−13.1	HC
83.78	3.29	20.0	22.3	−2.7	HC; S112

TABLE 1—*Continued*

l (1)	b (2)	T_b (3)	FWHM (4)	V_{LSR} (5)	Comments (6)
84.00	0.80	28.8	18.2	−8.7	GB
84.00	−0.60	49.0	18.7	−3.9	HC
84.21	1.84	5.5	26.9	−5.0	GB; 2c
84.21	1.84	6.9	18.0	−82.3	GB; 2c
84.42	1.26	14.7	13.7	−107.6	GB; 2c
84.42	1.26	23.4	25.6	−1.5	GB; 2c
84.50	−1.25	82.0	20.4	0.9	HC
84.60	1.84	10.4	11.6	−5.7	GB
84.60	−0.60	129.0	19.6	−2.8	HC
84.82	3.76	57.0	27.4	−5.3	HC; S115
84.86	−2.83	15.1	24.1	5.0	GB
85.10	3.85	66.0	22.8	−3.7	HC
85.46	−1.95	21.0	27.5	3.5	HC
85.80	−0.60	88.0	16.9	−3.9	HC
86.16	−1.25	30.0	30.5	−2.4	HC
88.00	−4.30	20.0	18.3	5.2	HC
90.88	1.88	13.0	22.0	−78.0	HC
90.93	1.54	15.7	21.5	−78.1	GB
91.00	0.00	(6)	0.0	0.0	HC
91.00	0.60	(6)	0.0	0.0	HC
91.00	1.20	(6)	0.0	0.0	HC
91.00	1.80	(6)	0.0	0.0	HC
91.00	2.40	(6)	0.0	0.0	HC
91.00	−0.60	(6)	0.0	0.0	HC
91.00	−1.20	(6)	0.0	0.0	HC
91.03	1.74	14.8	29.2	−79.2	GB
91.06	1.87	14.7	22.8	−79.4	GB
91.11	1.57	7.9	21.5	−11.5	GB; 2c
91.11	1.57	16.1	25.8	−76.8	GB; 2c
93.34	1.74	12.0	15.7	−74.1	HC
94.50	−1.54	28.4	22.2	−34.2	GB; S124
95.02	−1.92	16.3	17.9	−40.3	GB
95.40	−0.60	20.0	20.0	−21.6	HC; W
96.20	3.38	(2)	0.0	0.0	GB
96.60	3.38	4.9	29.6	−66.7	GB
99.43	4.37	29.0	21.4	−2.7	HC
102.60	−0.60	43.0	17.1	−47.0	HC; W
102.88	−0.60	32.0	20.9	−48.0	HC; S132; W
104.19	2.80	8.1	24.1	−11.5	GB; S134
105.74	0.18	8.9	18.1	−48.3	GB; near S138
107.09	−0.89	21.0	28.2	−40.0	HC; S142
107.50	5.25	23.9	21.6	−2.9	HC
108.60	3.04	(7)	0.0	0.0	GB
110.40	−0.60	21.0	42.7	−60.4	HC
113.40	−0.60	18.0	31.2	−55.7	HC; W
118.00	5.25	42.1	31.8	−7.0	HC
119.40	−0.60	19.0	20.0	−45.9	HC
121.80	−0.60	(11)	0.0	0.0	HC
136.80	0.60	42.0	9.8	−34.9	HC
151.06	−0.83	13.0	18.8	−23.2	HC
151.62	−0.25	16.0	26.3	−48.3	HC; S209
151.64	−0.50	(6)	0.0	0.0	HC
152.00	−0.60	(6)	0.0	0.0	HC
152.00	−1.20	(6)	0.0	0.0	HC
152.00	−1.80	(6)	0.0	0.0	HC
152.00	−2.40	(6)	0.0	0.0	HC
152.00	−3.00	(6)	0.0	0.0	HC
160.36	0.11	6.0	12.1	−26.7	HC; W
166.08	4.52	(5)	0.0	0.0	HC
167.65	−1.91	(6)	0.0	0.0	HC
168.72	0.99	(4)	0.0	0.0	HC; S227
172.30	−2.15	13.0	20.8	11.7	HC; near S229
173.35	−0.30	7.0	27.8	−23.4	HC; near S234
173.37	3.26	7.0	20.9	−22.1	HC; near S232; W
173.38	2.61	6.0	21.5	−16.2	HC; near S231
173.57	−1.76	31.0	25.9	−4.6	HC; near S236
173.60	2.79	13.0	15.2	−21.2	HC; near S235
190.06	0.50	37.0	17.9	5.4	HC; S252
192.63	−0.03	(4)	0.0	0.0	HC; S255
194.02	−1.83	22.0	8.7	4.2	HC
194.20	−2.03	(12)	0.0	0.0	HC
195.70	0.00	(4)	0.0	0.0	HC

TABLE 1—*Continued*

l (1)	b (2)	T_b (3)	FWHM (4)	V_{LSR} (5)	Comments (6)
200.63	2.06	4.0	12.8	9.3	HC; W
201.60	1.64	10.0	21.7	18.0	HC
202.00	1.80	10.0	21.0	10.7	HC
204.63	1.37	(5)	0.0	0.0	HC
208.81	−2.65	12.0	13.6	6.8	HC; S280
208.96	−19.36	70.0	22.0	−142.0	HC; Ori A, S281; 2c
208.96	−19.36	323.0	35.2	−6.8	HC; Ori A, S281; 2c
210.12	−2.30	(4)	0.0	0.0	HC; S282
210.63	−2.38	(5)	0.0	0.0	HC; S283
212.00	−1.23	(6)	0.0	0.0	HC
212.40	0.60	(6)	0.0	0.0	HC
213.00	0.60	(11)	0.0	0.0	HC
215.40	0.60	(6)	0.0	0.0	HC
216.00	0.60	(11)	0.0	0.0	HC
216.60	0.60	(6)	0.0	0.0	HC
219.00	0.60	(6)	0.0	0.0	HC
219.60	0.60	(8)	0.0	0.0	HC
220.20	0.60	(6)	0.0	0.0	HC
223.71	−1.91	13.0	15.1	15.5	HC; S292
223.93	−1.44	22.0	20.3	13.9	HC
224.33	−2.00	17.0	16.4	15.1	HC; S296
224.70	−2.47	13.0	19.1	17.9	HC
227.75	−0.15	(4)	0.0	0.0	HC; S298
228.00	−1.20	(6)	0.0	0.0	HC
228.00	−1.80	(7)	0.0	0.0	HC
228.00	−2.40	(6)	0.0	0.0	HC
228.00	−3.00	(6)	0.0	0.0	HC
231.49	−4.40	(5)	0.0	0.0	HC; S301
232.59	0.90	(5)	0.0	0.0	HC; S302
234.28	−0.40	(6)	0.0	0.0	HC; S306
234.63	0.72	8.0	31.5	39.4	HC; S307
235.55	−4.10	(4)	0.0	0.0	HC
253.80	−0.60	13.0	37.0	26.9	HC
254.40	0.60	(9)	0.0	0.0	HC
254.40	−0.60	(6)	0.0	0.0	HC
357.00	0.60	18.0	33.3	−4.4	HC
357.00	−0.60	23.0	32.6	2.9	HC; W
357.60	0.60	11.0	39.3	−1.8	HC; W
357.60	−0.60	23.0	20.5	4.8	HC
358.20	0.60	(6)	0.0	0.0	HC
358.20	−0.60	33.0	22.1	1.3	HC
358.39	−1.89	22.0	21.3	−4.5	HC
358.80	0.60	(21)	0.0	0.0	HC
358.80	−0.60	42.0	25.8	−5.1	HC
359.21	2.15	(4)	0.0	0.0	HC
359.40	0.60	136.0	17.9	1.2	HC
359.40	−0.60	55.0	29.5	3.5	HC
359.96	−17.76	24.0	23.3	8.4	HC

Cols. (1) and (2).—Galactic coordinates (degrees).

Col. (3).—Line intensity (units: brightness temperature in millikelvins). An entry in parentheses in col. (3) means no detection with the approximate upper limit of the entry.

Cols. (4) and (5).—Velocity FWHM and the LSR velocity (km s^{-1}).

Col. 6.—Comments: "GB" means that the position was observed at NRAO and HC at HCRO. An asterisk means that the position was observed at both GB and HC. A comment such as S37 means that the position is close to the H II region of that number in the catalog by Sharpless 1959. "2c," "3c," and "4c" mean that the spectra have respectively 2, 3, and 4 Gaussian components. "W" means that the detection is weak (see § 2.4). "Note 1": Spectra plotted and discussed in HKLR. "Note 2": This spectrum (l, b) = (31°50, −3°00) has an extraordinarily wide Gaussian fit. It may be more appropriately fitted by two Gaussians with (T_b, FWHM, V_{LSR}) = (6.3, 53.5, 44.2) and (6.6, 36.2, 105.0), but the signal-to-noise ratio does not warrant these extra parameters.

observations, repeating step 2, particularly if we thought that the position had particular significance. The term "particular significance" included, but was not limited to, the following cases: positions for which the RFRR source temperature was very small, to determine whether the RFRR source component is really a good indicator of thermal free-free emission; positions within a worm where other positions showed a detection, to determine whether the worm is a coherent structure not only in position but also in velocity; positions that appeared to show more than one velocity component.

Almost all of our suspected detections in step 2 were found to be real in step 3. This shows that our preliminary judgment of a detection was on the conservative side. If we did not repeat step 2 for an intermediate case—for example, because of unavailability of telescope time—then we made a second judgment about its reality and classified the result as

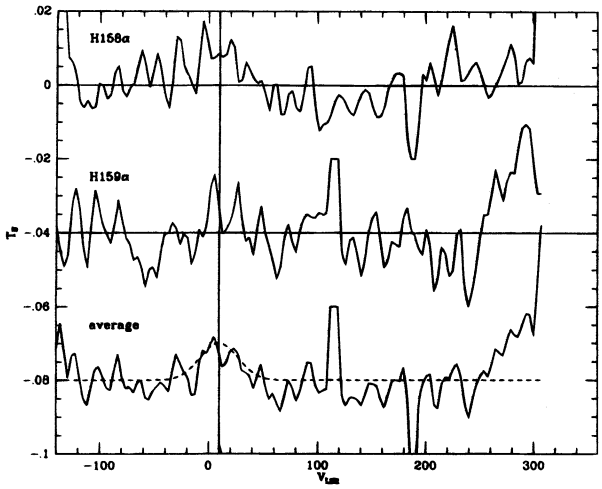

FIG. 1a

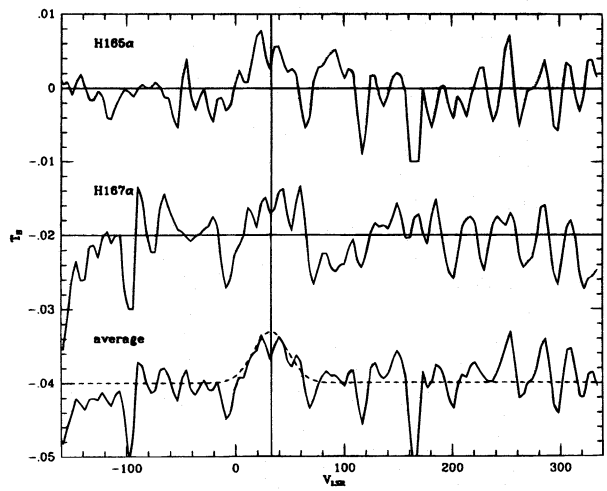

FIG. 1b

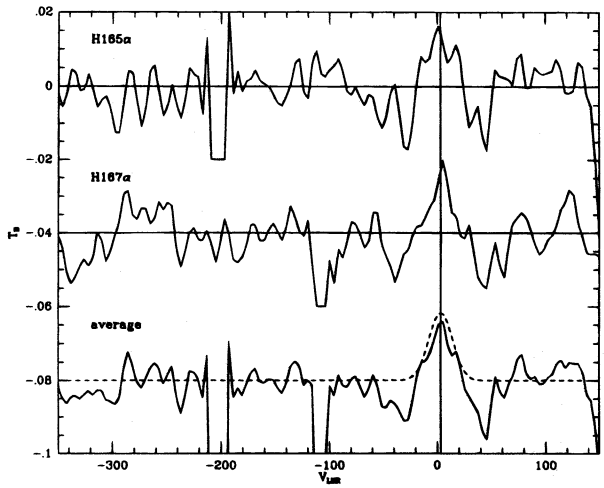

FIG. 1c

FIG. 1.—The typical signal-to-noise ratio for three "weak detections" (denoted by "W" in Table 1). For detections not so noted in Table 1, the signal-to-noise ratio is much better. For each of the three positions there are three spectra: the two spectra on top are the average of the two polarizations for the two RRL transitions, which were observed simultaneously. In the bottom spectrum, the solid line is the average and the dashed line is the Gaussian fit. At each position, the intensity scales for the three spectra are identical, but the zero levels have been displaced for clarity. All spectra are Hanning smoothed for clarity, but the Gaussians were fitted to the unsmoothed spectra. (*a*) $(l, b) = (10.^{\circ}7, -2.^{\circ}2)$. Gaussian parameters are $T_B = 10.0 \pm 3.0$ mK, half-width $= 38.7 \pm 9.3$ km s^{-1}, $V_{LSR} = 10.0 \pm 5.6$ km s^{-1}. For H158α (~1652 MHz), interference near 210 km s^{-1} reached −0.06 K; for H159α (~1621 MHz), interference near 110 km s^{-1} reached 0.10 K; without Hanning smoothing, interference of this strength produced no discernible ringing. The interference has been chopped off at $|T_B| = 0.02$ K for clarity. (*b*) $(l, b) = (15.^{\circ}0, -2.^{\circ}4)$. Gaussian parameters are $T_B = 7.0 \pm 1.8$ mK, half-width $= 36.8 \pm 7.3$ km s^{-1}, $V_{LSR} = 32.6 \pm 4.4$ km s^{-1}. For H165α (~1451 MHz), interference near 160 km s^{-1} reached −0.03 K; for H167α (~1400 MHz), interference near −100 km s^{-1} reached −0.02 K; without Hanning smoothing, interference of this strength produced no discernible ringing. The interference has been chopped off at $|T_B| = 0.02$ K for clarity. The presence of interference near 1451 MHz was unusual. (*c*) $(l, b) = (357.^{\circ}0, -0.^{\circ}6)$. Gaussian parameters are $T_B = 23.0 \pm 6.9$ mK, half-width $= 32.6 \pm 8.0$ km s^{-1}, $V_{LSR} = 2.9 \pm 4.4$ km s^{-1}. For H165α (~1451 MHz), interference near −200 km s^{-1} reached −0.78 K; for H167α (~1400 MHz), interference near −110 km s^{-1} reached −0.16 K; without Hanning smoothing, such strong interference produced severe ringing. The interference has been chopped off at $|T_B| = 0.02$ K for clarity. The presence of interference near 1451 MHz was unusual.

either a nondetection or a weak detection.

For the group of detections with smallest signal-to-noise ratio there is some uncertainty concerning the reality and considerable uncertainty in the derived Gaussian parameters. We mark these as "weak detections" with a "W" in Table 1. Figures 1*a*, 1*b*, and 1*c* exhibit three examples of weak detections. Each figure shows three spectra: the RRL at each of the two frequencies and also the average. In each case, it is the fact that the RRL is (marginally) detected independently at the two frequencies that allows us to classify it as a detection. These figures illustrate not only the typical weak detection but also the occasional problems with interference. The reader may believe that these spectra do not represent real detections and that we have been carried away by naivete and sophomoric enthusiasm. However, we have reasonably high confidence in these detections because of our experience developed during the above-described inspection process. Almost invariably, when we made further observations to confirm a suspected result at the level of these weak detections, we would find our suspicions confirmed. Obviously, we cannot guarantee that all of our "weak detections" are in fact real. However, our experience allows us to state confidently that nearly all of them are in fact real.

Further examples of weak detections appear in Figures 2*a*, 2*b*, and 2*c*, which show the weakest and least certain

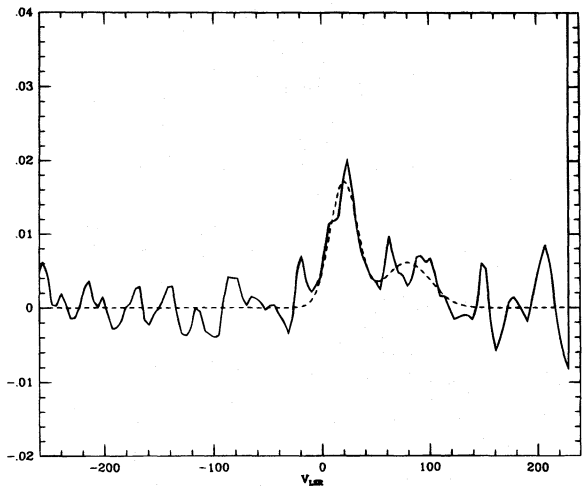

FIG. 2a

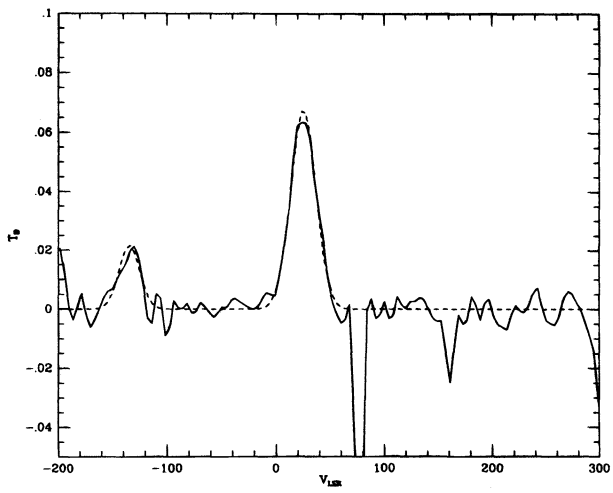

FIG. 2b

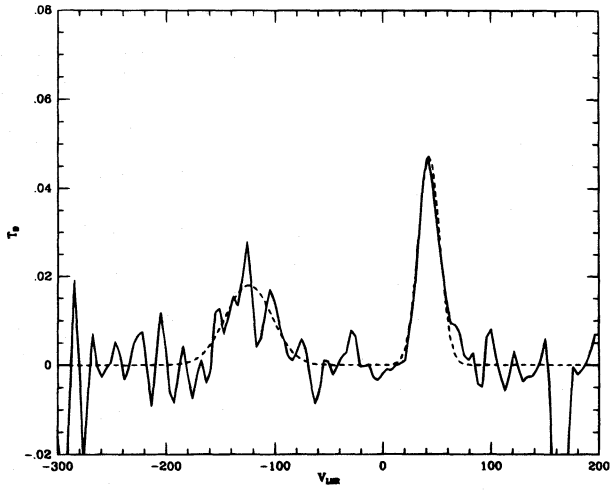

FIG. 2c

FIG. 2.—Weak examples of two-component detections (denoted by "W" and "2c" in Table 1) are illustrated. For each of the three positions the solid line is the average and the dashed line the Gaussian fit. All spectra are Hanning smoothed for clarity, but the Gaussians were fitted to the unsmoothed spectra. (*a*) $(l, b) = (13.^\circ41, 1.^\circ46)$. The broader Gaussian component was rated "W" in Table 1 and is correspondingly uncertain. Gaussian parameters are $T_B = 17.2 \pm 2.6$ mK, half-width $= 29.9 \pm 3.7$ km s^{-1}, $V_{LSR} = 20.7 \pm 2.6$ km s^{-1}; and $T_B = 6.1 \pm 2.2$ mK, half-width $= 49.6 \pm 14.6$ km s^{-1}, $V_{LSR} = 79.2 \pm 9.0$ km s^{-1}. (*b*) $(l, b) = (16.^\circ40, 0.^\circ63)$. Gaussian parameters are $T_B = 67.8 \pm 6.3$ mK, half-width $= 27.3 \pm 1.8$ km s^{-1}, $V_{LSR} = 25.3 \pm 1.2$ km s^{-1}; and $T_B = 21.7 \pm 6.9$ mK, half-width $= 22.1 \pm 5.2$ km s^{-1}, $V_{LSR} = -134.3 \pm 3.4$ km s^{-1}. The line at $V_{LSR} = -134.3$ km s^{-1} may correspond to a carbon RRL with $V_{LSR} = 15.4$ km s^{-1}. The interference near 80 km s^{-1} reached -0.10 K. (*c*) $(l, b) = (35.^\circ10, -1.^\circ50)$. Gaussian parameters are $T_B = 47.9 \pm 5.6$ mK, half-width $= 23.1 \pm 1.9$ km s^{-1}, $V_{LSR} = 42.4 \pm 1.3$ km s^{-1}; and $T_B = 18.0 \pm 3.8$ mK, half-width $= 49.7 \pm 7.7$ km s^{-1}, $V_{LSR} = -124.4 \pm 5.0$ km s^{-1}. The line at $V_{LSR} = -124.4$ km s^{-1} may correspond to a carbon RRL with $V_{LSR} = 25.3$ km s^{-1}. The interference near 160 km s^{-1} reached -0.09 K.

two-component detections. In these cases, the existence of an RRL is unquestionable. However, our description in terms of two velocity components instead of only one is less certain.

For most entries in Table 1, the uncertainties in the Gaussian parameters are small. This is best illustrated by the uncertainties for typical weak detections as quoted in the captions for Figure 1: the fractional uncertainty in line intensity and width is less than 30% in every case. For typical detections, which are not classified as "weak," the uncertainties are much smaller.

3. ELECTRON TEMPERATURE OF THE ELDWIM

Figure 3 shows the velocity-integrated RRL intensity $T_{RRL} \equiv \int T_B\, dv$ versus RFRR's 11 cm "source component" brightness temperature $T_{B,s}$ smoothed to the angular resolution of the RRL observations. The ratio of these two provides the electron temperature in the emitting region:

$$T_{e,4} = 1.06\left(\frac{f_{\rm NLTE}}{T_{\rm RRL}/T_{B,s}}\right)^{0.87}, \quad (1)$$

which applies for our case with the RRLs observed at 1.4 GHz and the continuum observed at 2.7 GHz. Here we have assumed that He is negligibly ionized in accordance with the results of HKLR. $T_{e,4}$ is the electron temperature in units of 10^4 K, and $f_{\rm NLTE}$ accounts for non-LTE effects in the line emitting process. The theoretical determination of the factor $f_{\rm NLTE}$ is reviewed by HKLR, who find $f_{\rm NLTE} \sim 0.9(1 + 0.021T_B)$, where T_B is the total 1.4 GHz continuum brightness incident on the emitting region from behind; typically, $T_B \sim 20$ K, which makes $f_{\rm NLTE} \sim 1.3$. Observationally, HKLR find that the higher order RRL intensities do not always correspond to theoretical prediction. Thus, we regard the theoretical estimate of $f_{\rm NLTE}$ with some

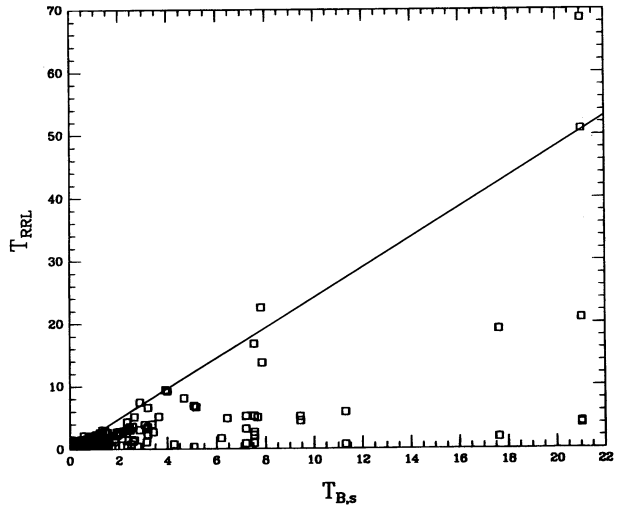

FIG. 3.—Integrated RRL intensity $T_{RRL} \equiv \int T_B dv$ vs. RFRR's 11 cm continuum "source component" $T_{B,s}$ for all points in Table 1; units are K km s^{-1} and K, respectively. The line is intended to approximately delineate the left-hand envelope and corresponds to $T_{e,4} f_{NLTE}^{-0.87} = 0.49$.

suspicion, but for lack of a better strategy we adopt $f_{NLTE} \approx 1.3$.

The points in Figure 3 scatter widely. However, they are distributed with a fairly well-defined left-hand envelope. Points move to the right on Figure 3 if some of the continuum temperature is nonthermal. Thus, the existence of the left-hand envelope corresponds well with the idea that T_{RRL} is well correlated with the *thermal* portion of the RFRR source component and has a fairly well-defined electron temperature, but that RFRR's source component also contains synchrotron radiation, which is unrelated to the thermal emission.[6]

[6] To be complete, we must note that points with larger T_e also move to the right on Fig. 3. We could alternatively interpret the left-hand envelope on Fig. 3 to mean that all the continuum is thermal but that the ELDWIM has a well-defined *lower* limit in T_e. We discount this alternative because it would require huge variations in T_e toward higher values, which is unlikely (see subsequent discussion in § 3).

This idea is corroborated by results for the Stockert chimney (which is part of GW 18.5+2.8, discussed below in §§ 5.2 and 6.1). Müller, Reif, & Reich (1987, hereafter MRR) determined the radio-continuum spectral index for this structure and showed that all of the chimney radiation is thermal. Figure 4*a* shows our observations for this region ($l = 18°$–$19°$, $b > 0°$). Our points cluster extremely tightly around the straight line on Figure 4*a* (which is an eyeball estimate, not a least-squares fit). We conclude that the scatter in Figure 3 is indeed a result of synchrotron radiation and that it is the left-hand envelope, rather than the centroid of the observed points, which has significance for the physical conditions in the emitting regions.

We can use the slope of the left-hand envelope to obtain the electron temperature. Figure 3, which includes all positions from Table 1, also shows a line which is intended to be a reasonable approximation to the left-hand envelope. For this line, $T_{e,4} = 0.49 f_{NLTE}^{0.87}$. Figure 4*b* shows only the less intense positions from Table 1, which should be more representative of the ELDWIM, together with the same straight line shown in Figure 4*a*; this line is a reasonable approximation to the left-hand envelope. The straight line in Figures 4*a* and 4*b* is shallower than that in Figure 3 and corresponds to $T_{e,4} = 0.58 f_{NLTE}^{0.87}$; if $f_{NLTE} = 1.3$, then $T_{e,4} = 0.73$.

MRR also determined the electron temperature for the Stockert chimney, and comparing their result with ours requires some discussion. In the text of their paper, they state that $T_{e,4} = 0.4$, which is much smaller than our result. However, the average electron temperature in their Table 5 is $T_{e,4} = 0.57$, which may be more representative of the observed values. Furthermore, while MRR assumed that He is ionized with $n_{He^+}/n_{H^+} = 0.12$, we assume He is neutral with $n_{He^+}/n_{H^+} = 0$ because of the results of HKLR. Using our assumption, the electron temperature as stated in MRR's text becomes $T_{e,4} = 0.44$, and the average of MRR's Table 5 becomes $T_{e,4} = 0.63$, in better, and perhaps satisfactory, agreement with our result.

We now compare our determinations of T_e for the ELDWIM with other previous results. Cersosimo (1990a) compared T_{RRL} with values of continuum brightness tem-

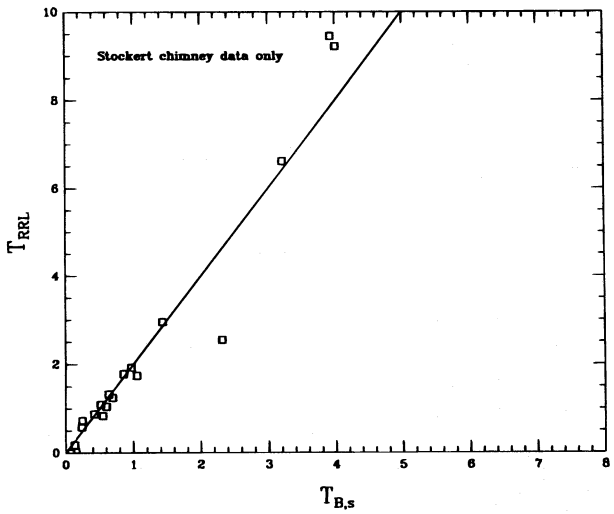

FIG. 4*a*

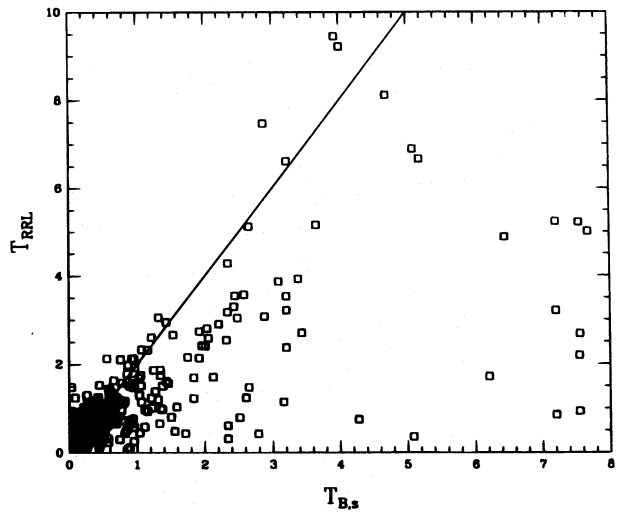

FIG. 4*b*

FIG. 4.—(*a*) Integrated RRL intensity $T_{RRL} \equiv \int T_B dv$ vs. RFRR's 11 cm continuum "source component" $T_{B,s}$ for the Stockert chimney in Table 1 ($l = 18°$–$19°$, $b > 0°$); units are K km s^{-1} and K, respectively. The line is an eyeball fit and corresponds to $T_{e,4} f_{NLTE}^{-0.87} = 0.58$. (*b*) Identical to Fig. 3, but with expanded scales: T_{RRL} vs. $T_{B,s}$ for the less intense points in Table 1; units are K km s^{-1} and K, respectively. The line is the same as in (*a*) and corresponds to $T_{e,4} f_{NLTE}^{-0.87} = 0.58$.

perature that were estimated indirectly and obtained $T_{e,4} = 0.67$. This seems to be good agreement, but it is not: he assumed $f_{\rm NLTE} = 1$ and $n_{\rm He^+}/n_{\rm H^+} = 0.10$. If he had used our values for these parameters, he would have obtained $T_{e,4} = 0.91$, considerably larger than our value of 0.73. We suspect that the disagreement lies in his method for estimating continuum temperatures. Apart from this and MRR's determination, we know of no other previous determinations that use the ratio of RRL to continuum intensities as in equation (1). We know of two other techniques. The first technique uses RRL widths to establish upper limits on T_e, which makes the upper limits very reliable: Shaver et al. (1983) found $T_{e,4} < 0.36$ for $(l, b) = (24.^\circ5, -0.^\circ2)$ and $(24.^\circ7, -0.^\circ2)$, and Lockman (1989) found 14 objects with $T_{e,4} < 0.46$ (one of which had $T_{e,4} < 0.29$). With the second technique, Lockman (1980) derived $T_{e,4} \lesssim 0.3$ for the ELDWIM at $(l, b) = (36^\circ, 0^\circ)$ by comparing the thermal continuum intensity in this direction with a representative value for the thermal continuum optical depth as determined for other directions. We view Lockman's result with some suspicion because the optical depth he used is not relevant to this particular position. If the optical depth for that position is approximately half the value that Lockman adopted, then his $T_{e,4}$ would be comparable to ours. Such a smaller optical depth is not unlikely because the thermal continuum emission in this particular direction is among the lowest in the Galactic plane. Indeed, Lockman also presents RRL data for this particular direction, and a comparison of his RRL intensity with the thermal continuum intensity using equation (1) yields $T_{e,4} \approx 0.49 f_{\rm NLTE}^{0.87}$. This is also smaller than our value $T_{e,4} = 0.58 f_{\rm NLTE}^{0.87}$, which may be significant and show that weaker positions have smaller electron temperatures; alternatively, the difference is fairly small and might be rationalized in terms of either observational uncertainty or "cosmic scatter."

Our result from the left-hand envelope in Figure 4*b*, $T_{e,4} = 0.73$, is much higher than the definitive upper limits of Shaver et al. (1983) and Lockman (1989). We explain this incompatibility in terms of a low rate of occurrence for their small values of T_e, because positions having $T_{e,4} < 0.73$ move to the *left* on Figure 4*b*. If there were many such points, then there could not possibly be a well-defined left-hand envelope.

To summarize: From our result $T_{e,4} = 0.58 f_{\rm NLTE}^{0.87}$, we adopt $T_{e,4} = 0.70$ (as a "round number" approximation) and $f_{\rm NLTE} = 1.28$ for the ELDWIM. For H II regions, Downes et al. (1980, hereafter DWBW) also find $T_{e,4} \approx 0.70$; the equality of these numbers argues that the heating, ionization, and cooling processes are the same for the ELDWIM and H II regions. The definitive upper limits $T_{e,4} < 0.36$ of Shaver et al. (1983) and $T_{e,4} < 0.46$ of Lockman (1989) show that there must exist fluctuations in T_e for the ELDWIM, but our well-defined left-hand envelope shows that fluctuations toward $T_{e,4} < 0.70$ are not common.

4. GALACTIC LOCATION, DENSITY, AND FILLING FACTOR OF THE ELDWIM

4.1. *Spiral Arms and the Velocity-Longitude Diagram for the ELDWIM*

If we make the standard assumption that the observed $V_{\rm LSR}$ is a result of differential Galactic rotation, then for each entry in Table 1 we can determine the Galactocentric radius $R_{\rm Gal}$ and, within the usual twofold ambiguity, the distance from the Sun, $d_\odot$. Here we use the rotation curve and standard Galactic parameters given by Burton (1988). In addition, TC have used pulsar dispersion measures to identify three components of ionized gas in the Galaxy: the inner Galaxy ringlike, outer disk ringlike, and spiral arm components. We will compare our results to theirs. Furthermore, we will begin by using TC's characterization of the classical spiral arms of Georgelin & Georgelin (1976), which are defined by H II regions; later we will propose a small revision. TC designate the spiral arms by numbers 1–4, with increasing number corresponding to increasing $R_{\rm Gal}$.

Figure 5 shows four velocity-longitude plots. On each plot we indicate regions of the Galaxy that will be important in our ensuing discussion: TC's four spiral arms are shown with dotted lines; TC's ringlike inner Galaxy component is bounded by $2.2 \lesssim R_{\rm Gal} \lesssim 5.2$ kpc and is shown by short-dashed lines; most of our RRL detections lie outside $R_{\rm Gal} \gtrsim 4.3$ kpc, which is shown by a long-dashed line; and the "tangential point" velocity $V_{\rm max}$ is shown with a solid line.

Figure 5*a* shows the RRLs of radio-observed H II regions from DWBW, whose survey covered *strong* H II regions and covered only $l < 60^\circ$. Figure 5*a* shows that the strong H II regions are concentrated in the spiral arms to some degree. The correlation not only exists but also is a tautology, because the spiral arms are defined by these H II regions (Georgelin & Georgelin 1976). Nevertheless, the concentration of the H II regions to spiral arms is not complete, either because velocity dispersion spoils an otherwise perfect concentration or because the concentration is in fact imperfect. One point is distinctly clear: Figure 5*a* shows that the distribution of strong H II regions is not ringlike, because the diagram contains areas that are distinctly empty.

We conclude that TC's inner Galaxy component, which is ringlike, is not associated with strong H II regions. To underscore this point, Figure 5*b* presents a simulation and shows a pseudorandom distribution of H II regions that would be observed if the surface density of H II regions were proportional to $\langle n_e \rangle^2$ for TC's ringlike inner Galaxy component (TC's eq. [16]). The points have obvious concentrations toward the tangent points and near $l = 0^\circ$, but distinctly empty areas do not exist. Furthermore, the points are concentrated toward smaller Galactocentric radii than are the H II regions.

Figure 5*c* shows the velocity-longitude diagram for our RRLs. The ELDWIM points scatter more uniformly than do the strong H II region points, but there remain three prominent empty regions centered near $(l, V_{\rm LSR}) = (23^\circ, 40$ km s^{-1}), $(32^\circ, 68$ km s^{-1}), and $(47^\circ, 33$ km s^{-1}). In addition, for the ELDWIM there is only a handful of points inside $R_{\rm Gal} \lesssim 4.3$ kpc; in contrast, for strong H II regions the density of points on Figure 5*a* decreases inside 4.3 kpc but does not go to zero until $R_{\rm Gal} \lesssim 3.7$ kpc. We conclude that the ELDWIM is not very well correlated with strong H II regions.

In Figure 5*d* we plot the RRLs of the mostly *weak* H II regions in Lockman's (1989) survey, which covers the full longitude range shown. Again there are relatively empty regions outside spiral arms that imply some concentration to spiral arms, but significantly less concentration than for the strong H II regions. Figure 5*c* seems similar to Figure 5*d*: it shows the same three empty regions, and the distribution of points looks roughly similar. There are differences: a

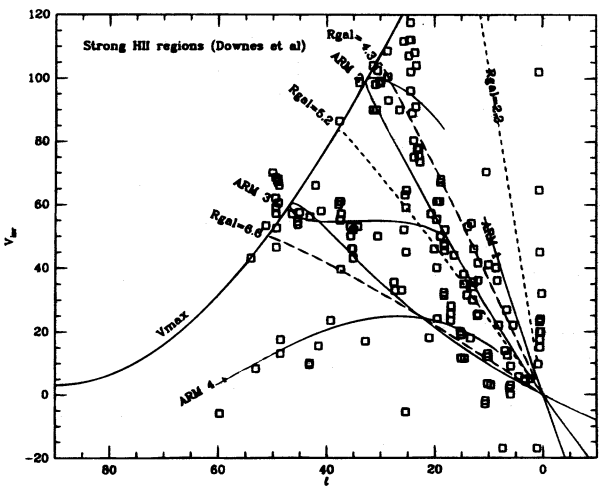

FIG. 5a

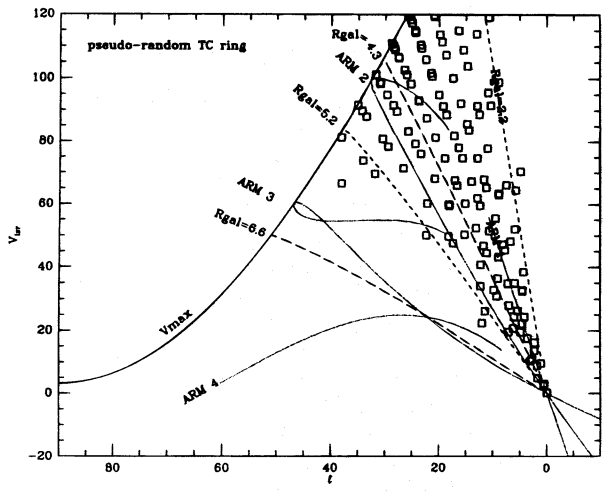

FIG. 5b

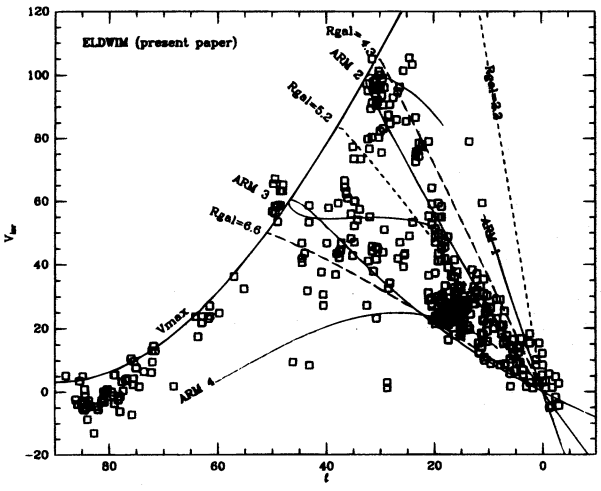

FIG. 5c

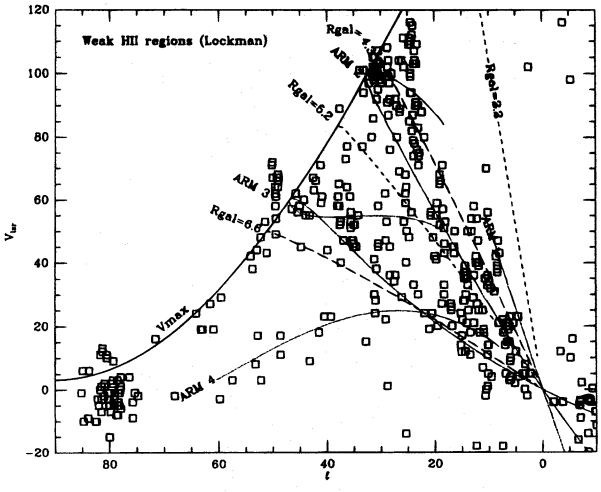

FIG. 5d

FIG. 5.—(*a*) Velocity vs. longitude (V_{LSR} vs. l) for the *strong* H II regions of DWBW. DWBW's H II region catalog is restricted to $l < 60°$, so the absence of points for $l > 60°$ is meaningless. The dotted lines locate the four spiral arms defined by TC. The short-dashed lines delineate the annulus of the Galaxy that contains TC's azimuthally symmetric inner Galaxy electron component (2.2 kpc $< R_{Gal} <$ 5.2 kpc), which we argue does not exist (§ 4.2). The long-dashed lines delineate the annulus (4.3 kpc $< R_{Gal} <$ 6.6 kpc); the ELDWIM lies mainly outside $R_{Gal} \gtrsim 4.3$ kpc. The solid line labeled V_{max} delineates the "tangential point" velocity. (*b*) Velocity vs. longitude (V_{LSR} vs. l) for a psuedorandom set of points whose areal density in the Galactic disk is proportional to the $\langle n_e \rangle^2$ of TC's inner Galaxy electron component (TC's eq. [16]). The lines are as in (*a*). (*c*) Velocity vs. longitude (V_{LSR} vs. l) for all points in Table 1. The lines are as in (*a*). (*d*) Velocity vs. longitude (V_{LSR} vs. l) for the *weak* H II regions of Lockman (1989). The lines are as in (*a*).

few ELDWIM points lie outside regions where weak H II regions lie, specifically near (l, V_{LSR}) = (40°, 30 km s^{-1}), and weak H II regions extend to smaller R_{Gal} than the ELDWIM. The similarity suggests that the ELDWIM may be associated with weak H II regions. We emphasize that this is a suggestion, not a definitive conclusion. A definitive conclusion requires a thorough statistical analysis because the density of points is high, but this is beyond the scope of the present paper.

To summarize: Neither the ELDWIM nor the H II regions are distributed in rings because the density of points changes too much along lines of constant R_{Gal}. This point has been made before, by Cersosimo et al. (1989) for the ELDWIM and by Lockman (1979) for bright H II regions. This also applies to the CO distribution: the Galactic "molecular ring" is not really a ring, but more likely spiral arms (Combes 1991). Both the strong and weak H II regions, and in particular the ELDWIM, do not extend farther in than $R_{Gal} \sim 3.7$ kpc. The ELDWIM may be associated to some degree with H II regions, which are in turn associated with the spiral arms.

The Galactic distribution of the H II regions and ELDWIM contrasts with the TC inner Galaxy component 2. Not only is TC component 2 ringlike, but it also extends in to $R_{Gal} \sim 2.2$ kpc. We conclude that the TC component 2—if it exists—is different from the electrons that produce the RRLs from H II regions and the ELDWIM.

4.2. *TC's Ringlike Inner Galaxy Component: Is It Real?*

Our results above (§ 4.1) show that TC's inner Galaxy ring component of electrons does not produce observable RRLs, which implies an upper limit on its emission measure (EM). From Table 1, we see that a fairly conservative estimate for our sensitivity limit is $\int T\,dv \sim 0.2$ K km s^{-1}. We adopt this value as the upper limit for RRL emission from the ring component. For $T_{e,4} = 0.58 f_{NLTE}^{0.87}$ (§ 3), this corresponds to EM $\lesssim 220$ cm^{-6} pc. For a representative line of sight through the ring where we see no RRL emission at,

say, $l = 20°$, the dispersion measure (DM) produced by the ring alone, for both the far and near portions, amounts to $\mathrm{DM} \equiv \int n_e\, dl \sim 800\ \mathrm{cm}^{-3}$ pc. In the usual description of the ELDWIM, electrons are clumped into clouds all of which have the same electron volume density n_c with volume filling factor ϕ_{WIM}, and we have

$$\phi_{\mathrm{WIM}} = \langle n_e \rangle \mathrm{DM}/\mathrm{EM}\ . \tag{2}$$

We take $\langle n_e \rangle = 0.05$, which is half the peak value in TC's ring, and find $\phi_{\mathrm{WIM}} \gtrsim 0.20$.

This is a large filling factor for the WIM. It far exceeds the value $\phi_{\mathrm{WIM}} \approx 0.09$ observed at $z = 0$ for the solar neighborhood (Reynolds 1991). Thus, the absence of RRL emission from the ring implies that its distribution of electrons is extraordinarily smooth. This, in contrast, is incommensurate with the strong scattering that is associated with this component.

We briefly review the essentials of interstellar scattering. Interstellar scattering of pulsars results from very small perturbations in electron density, δn_e, on very small length scales. The observations indicate that these follow a Kolmogorov spectrum (see Cordes et al. 1991), in which the wavenumber spectrum for δn_e is a power law that runs between l_1 and l_0, the inner and outer length scales. The observational parameter that expresses the scattering power is called the scattering measure (SM). Cordes et al. (1991) provide straightforward expressions for SM for a simple model in which the electrons are distributed in clumps of density n_c. The clump-to-clump density varies as expressed by the parameter $\zeta = \langle n_c^2 \rangle / \langle n_c \rangle^2$, and within a single clump the electron density varies as expressed by the parameter $\epsilon = \delta n_{c,\mathrm{rms}} / \langle n_c \rangle$, where here the angular brackets indicate a volume average over the clump. TC combine these parameters in the "fluctuation parameter" $F = (l_0/\mathrm{pc})^{-2/3}(\zeta\epsilon^2/\phi_e)$, which is proportional to the observed SM/DM. In terms of these parameters, the observables for the clump model are related by

$$\mathrm{SM} = 1.84 \times 10^{-3} F \langle n_e \rangle \mathrm{DM} \tag{3}$$

and

$$l_0 = \left[\frac{\epsilon^2}{\phi_{\mathrm{WIM}} F (1 + \epsilon^2)} \right]^{3/2} \mathrm{pc}\ . \tag{4}$$

For the Galactic interior, TC find $F \sim 40$; the scattering is ~ 100 times more prominent than near the Sun. Above we obtained an approximate lower limit of $0.20\ \phi_{\mathrm{WIM}}$. The maximum value of ϵ is unity, so $l_0 \lesssim 0.014$ pc.

Thus, if the TC electron ring component is real, it has a large filling factor and the fluctuations exist only on length scales smaller than about 0.014 pc. The corollary is that the electrons are distributed smoothly. This is unlike any other known electron component—indeed, it is unlike the distribution of *any* interstellar component, because all exhibit significant clumping. It is more reasonable to assume that TC's inner Galaxy electron component does not exist.

We postulate that the TC inner Galaxy ringlike component is instead associated with TC's spiral arms 1 and 2. Such a modification of their model is quite plausible. TC's Figure 4 shows that these two spiral arms approach the TC ring tangentially and merge with it. From visual inspection of this figure, it seems clear that it is difficult to distinguish between electrons in their inner Galaxy ring and spiral arms 1 and 2. Observationally, this would require knowing fairly accurate distances $d_\odot$ to a reasonably large number of pulsars in the longitude ranges $10° \lesssim l \lesssim 40°$ in the first quadrant and $320° \lesssim l \lesssim 350°$ in the fourth. For $d_\odot$ TC used the list of Frail & Weisberg (1990), which contains lower and upper distance limits based mainly on 21 cm line absorption measurements to either the pulsar or an associated supernova remnant. Within the range $10° \lesssim l \lesssim 40°$, this list contains 12 pulsars, but for only four of these pulsars to the upper and lower distance limits lie reasonably close ($\sim 40\%$) to each other. Within the range $320° \lesssim l \lesssim 350°$, the list contains only three pulsars, with only one for which the limits are close. In our opinion, too few accurate pulsar distances are known to distinguish between the ring and arm distribution possibilities, and the absence of RRL emission from TC's postulated ring argues strongly that it does not exist.

4.3. *A Working Model for the Electron Distribution: Concentration to Slightly Revised Spiral Arms*

We wish to develop a working model for the electron distribution, without performing an extensive reanalysis of the pulsar DM data, by proposing the smallest revision to the TC model that makes it physically plausible and reasonably consistent with the above. Broadly speaking, a working model should retain the electron column densities found by TC, which are accurately derived from pulsar DMs; should relocate the electrons into spiral arms, which is permissible because most of the pulsar distances are inaccurately known; and should minimize the distance that the electrons are moved.

1. We eliminate the Galactic quadrant 1 (Galactocentric quadrant 2)[7] portion of TC's arm 1; with this, the electrons in arm 2 dominate the first Galactic quadrant, and those in arm 1 dominate the fourth Galactic quadrant. We accomplish this by chopping off the innermost 38° in θ of arm 1, which is the dashed part of the arm pictured on Figure 6*a*. (Here θ is the same "Galactic azimuth" as defined by TC.) With this choice, both arm 1 and arm 2 begin at the same $R_{\mathrm{Gal}} \approx 3.77$ kpc. Chopping off the inner end of arm 1 is not at all unreasonable because it simply eliminates one particular clump of H II regions from arm 1. These H II regions are all associated with W31, which has an anomalous velocity with respect to the rest of arm 1. As summarized in § 5.1 below, the data for W31 do not fit well with pure circular rotation, and W31 may lie in the "3 kpc arm."

2. We eliminate TC's inner Galaxy ringlike component of electrons and put them into spiral arms 1 and 2 in a manner that retains the total measured DMs at $b = 0°$. For $63° < \theta \lesssim 190°$, which corresponds to Galactic quadrant 1, we move the ring electrons into arm 2. For $190° < \theta \lesssim 330°$, which corresponds to Galactic quadrant 4, we move the ring electrons into arm 1. With this choice, arms 1 and 2 contain the enhanced ring component out to $R_{\mathrm{Gal}} = 5.81$ and 5.37 kpc, respectively; we have moved the original ring electrons out to the range $3.8 \lesssim R_{\mathrm{Gal}} \lesssim 5.6$ kpc.

3. We retain the radial and the z extents of the inner Galaxy component by assuming that the radial and z distributions in these portions of arms 1 and 2 are appropri-

[7] The term "Galactic quadrant" is the standard definition in terms of Galactic longitude, centered on the Sun. Below we will also use the term "Galactocentric quadrant," which is defined in terms of the Galactocentric angle θ, the "Galactocentric azimuth" measured counterclockwise around the Galactic center (see Fig. 6*a*).

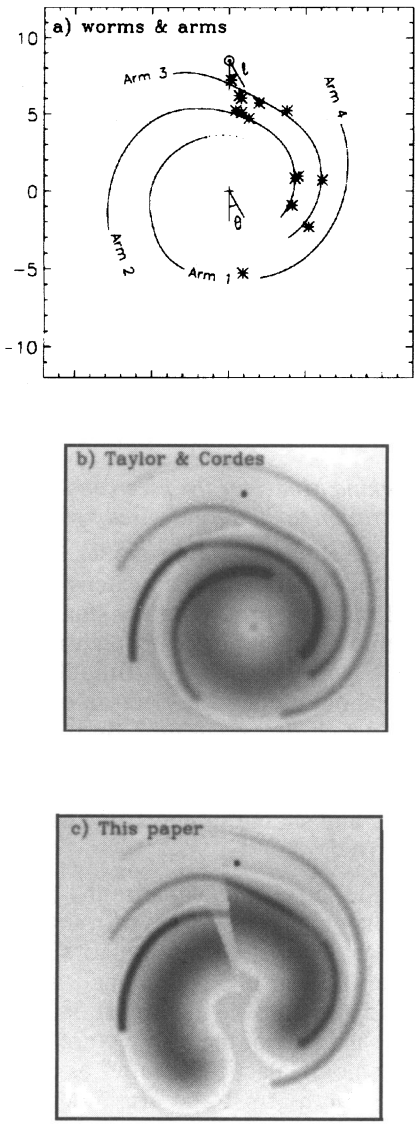

FIG. 6.—Face-on views of the Galaxy. (*a*) Locations of spiral arms from TC and Georgelin & Georgelin (1976) are shown as solid lines, with the portion of arm 1 we have removed shown as dashed (§ 4.3). Asterisks locate the worms from Table 4. This figure also defines the Galactic longitude l and the Galactocentric azimuth θ. The linear scale is centered on the Galactic center and is in units of kiloparsecs. (*b*, c) Gray-scale images of the electron volume density at $z = 0$ for (*b*) TC's model and (*c*) our revised "working model" of § 4.3. The primary differences are that we placed the electrons from TC's inner Galaxy "ring" into arms 1 and 2, and we made arms 1 and 2 thicker. The odd "pie-shaped" discontinuity occurs because we endeavored to retain a continuous electron column density *Galactic longitude* in order to maintain maximal correspondence with the *observations.*

ately weighted averages of TC's original spiral arm and inner Galaxy ring components.

Above we have specified the relocation of the ring electrons for the range $63° < \theta < 330°$. This leaves unspecified the remaining interval $-30° < \theta < 63°$. This is the portion of the TC ring that lies beyond the Galactic center in the range $-12° < l < 18°$. Our revision of TC's model makes the unlikely implicit assumption that the ring electrons do not exist in this region, because there is no known spiral arm with $R_{\rm Gal} \lesssim 5.9$ kpc in this longitude interval. The nonexistence of ring electrons here is not inconsistent with the pulsar data, because pulsars with large DMs are very sparse in this longitude interval: there are only two pulsars with DM > 600 cm^{-3} pc there (Clifton & Lyne 1986; Johnston et al. 1992). More definite statements about this awkward, poorly mapped part of the Galaxy must await more data.

The following list specifies the details of our proposed working model for the global electron distribution:

1. We retain TC's "outer disk" component as summarized in their Table 2 with the parameters subscripted 1. This component is the one responsible for pulsar DM near the Sun. It has $h_1 = 0.88$ kpc, scale length in $R_{\rm Gal} = 20$ kpc, and $\langle n_e \rangle = 0.019$ cm^{-3} near the Sun.
2. The remaining electrons are located in spiral arms.
3. Shapes of spiral arms are derived from TC's Table 1 using the "natural cubic spline" and subroutines SPLINE and SPLINT (Press et al. 1989). However, our arm 1 covers only the range $202° < \theta < 330°$.
4. In arm 1 at $z = 0$ for $\theta \geq 202°$, n_e is given by

$$n_e = 0.114 \exp\,[-(d_a/1.8)^2]\ \text{cm}^{-3}\ , \qquad (5)$$

where d_a is the distance from the axis of the spiral arm in kiloparsecs. This corresponds to the entire length of arm 1.
5. In arm 2 at $z = 0$ for $\theta \leq 190°$, n_e is given by equation (5). This corresponds to the inner portion of arm 2 ($R_{\rm Gal} < 5.37$ kpc). In the remainder of arm 2, n_e is as given by TC.
6. For arms 1 and 2 in the regions of θ where equation (5) applies,

$$n_e(z) = n_e(0)[0.12\ \text{sech}^2\ (z/h_a) + 0.88\ \text{sech}^2\ (z/h_2)]\ , \qquad (6)$$

where h_a and h_2 are TC's original scale heights for the spiral arm and inner ring components; $h_a = 300$ pc and $h_2 = 150$ pc. Elsewhere, $n_e(z)$ is as given by TC.
7. In arms 3 and 4, n_e is the same as given by TC's § 3.1 and Table 2.

Figure 6*c* exhibits this proposed working model, and Figure 6*b* the TC model from which it was derived. Note the odd "pie-shaped" discontinuity in Figure 6*c*. This occurs because we endeavored to retain a continuous electron column density versus *Galactic longitude*, so as to maintain maximal correspondence with the *observations*. Thus our model is an *empirical* model designed to be consistent with the observations. It is not intended to reflect the effect of real *physical processes*.

4.4. *Problems with Our Working Model*

Our working model is inconsistent with the fact that we detect very little ELDWIM for $R_{\rm Gal} \lesssim 4.3$ kpc. Arms 1 and 2 extend in to $R_{\rm Gal} \approx 3.8$ kpc; thus, RRLs should be observable this far in—actually, somewhat farther (to $R_{\rm Gal} \sim 2.8$ kpc) because the full width of the arms as measured in n_e^2 is about 2 kpc. Thus, our working model predicts the density of RRL points on Figure 5*c* to be high as far in as $R_{\rm Gal} \sim 2.8$ kpc, contrary to observation.

This difficulty with our working model results from our original goal in its production, namely, to perturb the original TC model as little as possible. Our working model puts the electrons at larger $R_{\rm Gal}$ than does the TC model, but they should be moved out even farther. Developing a more realistic model requires detailed analysis of pulsar DMs; SMs derived from pulsars, Galactic OH masers, and extragalactic continuum sources; and EMs derived from thermal radio continuum and RRL measurements. Ancillary data

include far-IR lines, dust emission, and H I. Current models of the Galactic electron distribution are based on various subsets of these data, and no model fits the full set of data very well. We believe that the time is ripe for an extensive reanalysis, but such a task is well beyond the scope of the present paper.

For now, we adopt our above-described model. We can make one firm prediction, which is based on the discrepancy between the radial locations of the ELDWIM as defined by RRL emission and as defined by pulsar DMs: the distances for the inner Galaxy pulsars have been overestimated, placing the pulsars at smaller $R_{\rm Gal}$ than they really are. This prediction can be directly verified only by measuring the distances to these pulsars independently, e.g., by using the 21 cm line absorption technique.

4.5. *The Filling Factor and Electron Density of the ELDWIM*

As explained above, in our working model the spiral arm electrons produce most of the pulsar dispersion and all of thermal radio emission, which allows us to derive the filling factor. For this purpose, we consider $l = 20°$. This lies just outside the inner $R_{\rm Gal}$ boundary of arm 2, where the line of sight makes two passes through arm 2, one on the "near" side and one on the "far." At higher longitudes the line of sight becomes tangential to arm 2, which produces an obvious rise in both the RRL and thermal radio continuum intensity (see Fig. 2 of Mezger 1978). Also, at these higher longitudes the DM produced by this tangential line of sight is large and has large uncertainties, as indicated by the fact that contours of DM become nearly parallel to the line of sight for large distances (see Fig. 5 of TC).

At $l = 20°$, Mezger's Figure 2 shows that the 1.4 GHz thermal radio continuum has $T_B \approx 8.5$ K, which with $T_{e,4} = 0.7$ gives EM ≈ 4200 cm^{-6} pc. TC's Figure 5 shows that the total DM produced after the two passes through arm 2 is DM ~ 1000 cm^{-3} pc. About 200 cm^{-3} pc of this is produced by TC's outer disk component, leaving the DM assignable to the spiral arm component as 800 cm^{-3} pc. Combining these using equation (2) gives the volume filling factor of the ELDWIM within the spiral arm region,

$$\phi_{\rm WIM} \sim 0.011 , \tag{7}$$

where we have adopted $\langle n_e \rangle = 0.057$ cm^{-3}, which is half the peak value in the spiral arms according to our working model. The fact that we included only the spiral arm component contribution to the DM and EM means that $\phi_{\rm WIM}$ refers to the fraction of spiral arms that is filled by electrons, not the fraction of the total line of sight. The electron density in the clumps is

$$n_c = \frac{\rm EM}{\rm DM} \sim 5.2 \text{ cm}^{-3} . \tag{8}$$

These parameters, which refer to $z = 0$, indicate a highly clumped medium, much more so than near the Sun, where $\phi_{\rm WIM} \approx 0.09$ at $z = 0$ (Reynolds 1991). The thermal pressure P/k is approximately 7×10^4 cm^{-3} K, roughly 16 times the local WIM pressure. This factor is much larger than expected from hydrostatic equilibrium: the radial exponential scale length of the Galaxy is 3.7 kpc (Bahcall, Schmidt, & Soneira 1983), and the overlying mass (which is mainly H I) is comparable (Dickey & Lockman 1990), so the hydrostatic equilibrium pressure should be only about 2.7 times larger than locally. The higher clumping and large pressure indicates that the ELDWIM is not in equilibrium, which is not surprising because it resides in a region where star formation and supernovae are rampant.

The total length along the line of sight occupied by clumps is $L = {\rm DM}^2/{\rm EM} \approx 150$ pc. These values agreee with the estimates by Anantharamaiah (1985), who used RRL observations at various frequencies to estimate $n_c =$ 1–10 cm^{-3} and $L \sim 100$ pc. There may be one large clump or many smaller clumps that, together, fill this length. There are no explicit data on the sizes of the clumps. There is one statistical piece of information, namely, that the intensity of thermal radio emission—represented by the map of $T_{B,s}$—is patchy. This argues that the number of clumps N along the line of sight is small enough for "root-N" statistics to exhibit observable fluctuations, which implies that the clumps are physically large. In our opinion, the clumps are probably $\sim$20–50 pc in thickness. At a typical distance to the regions we are observing, clumps of this size are comparable to the beamwidth, and because of small-number statistics this is consistent with the fact that we do not detect RRLs at some positions.

We return briefly to the scattering aspect of the ELDWIM, employing again our discussion in § 4.2. For $\phi_{\rm WIM} = 0.011$ and $\epsilon = 1$, equation (4) yields $l_0 \approx 1.1$ pc. This is much smaller than our preferred clump size of 20–50 pc and indicates that within the clumps there exist large variations in n_e—i.e., that the clumps are highly turbulent on scales $\lesssim 1.1$ pc. The physical process that produces the turbulence must operate on a scale comparable to this.

The remainder of this discussion is necessarily speculative. The $l \sim 20°$ line of sight goes once through arm 3 and twice through arm 2. If the electrons are equally divided among these arm crossings, then each arm contributes electrons that reside in a path of length 50 pc. In a minority of cases (§ 6.4), we believe that the emission arises from "worm walls." These are large structures, and a line of sight should usually intersect two walls as it passes through a worm. It seems quite reasonable to us that the thickness of a worm wall is approximately 25 pc, and there is no need for smaller clumping except as required by interstellar scattering. However, most of the time the electrons do not reside in worm walls. Mezger (1978), Lockman (1976, 1980), and Anantharamaiah (1986) consider that these more typical electrons reside in the outer parts of H II regions, forming an extended envelope. Again, it seems quite reasonable to us that the thickness of such a region is roughly 20–50 pc.

5. WORMS SEEN IN THERMAL RADIO CONTINUUM AND RRL EMISSION

5.1. *Our Worm Catalog*

Koo, Heiles, & Reach (1992, hereafter KHR) presented a catalog of 118 Galactic worm candidates. This catalog was based on the morphology of H I diffuse 100 μm emission, and diffuse 408 MHz continuum emission. The data presented in the present paper provide another tool with which to study these objects.

The "source component" of RFRR's 11 cm survey has a striking wormlike morphology, with structures that are primarily vertical (Heiles 1993a; Reach, Heiles, & Koo 1993). Similar structures appear in the "southern sky" (Galactic quadrant 4; Jonas, de Jager, & Baart 1985). Figure 7 presents gray-scale images of the "northern sky" RFRR source

1996ApJ...466..191H

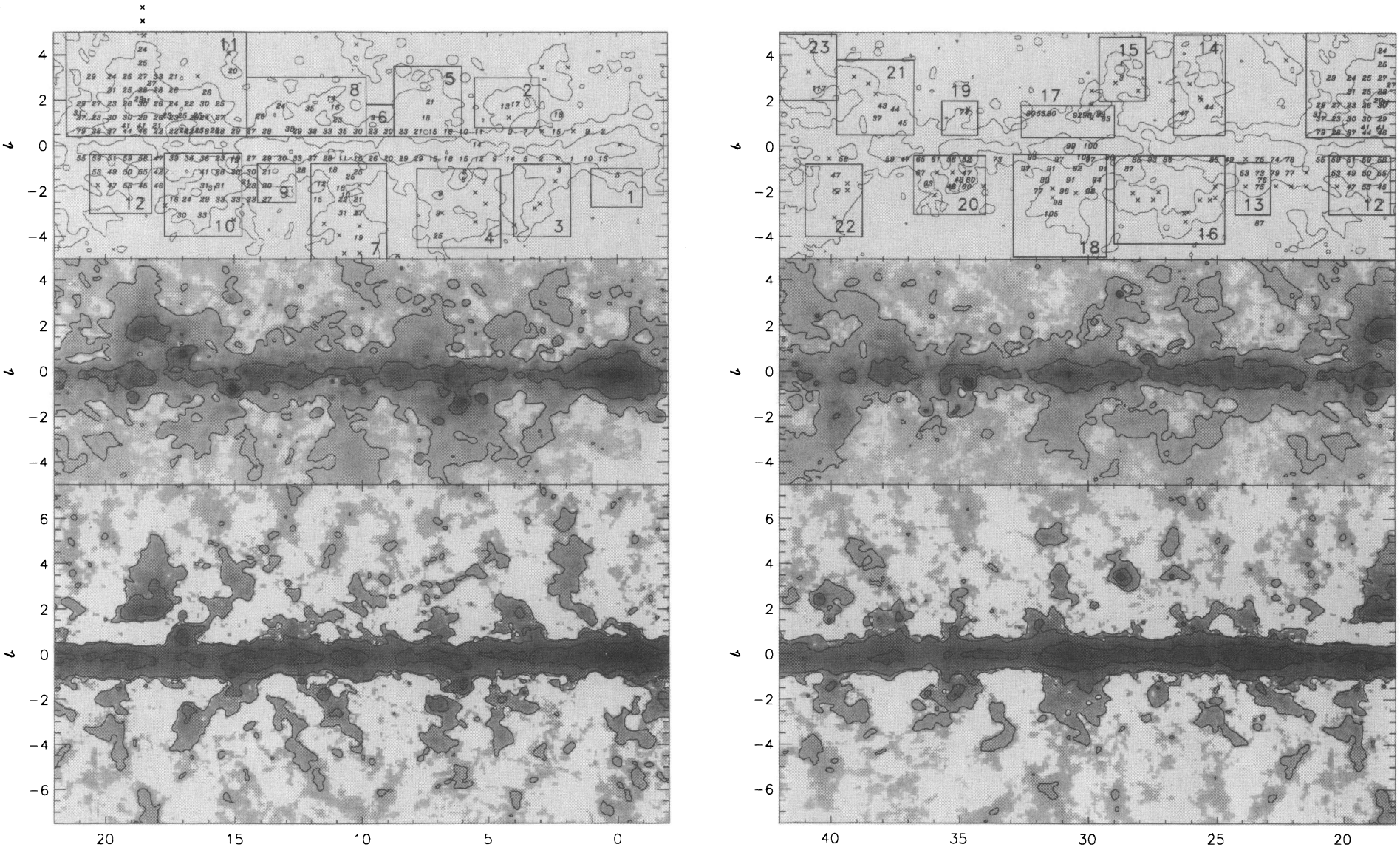

FIG. 7.—*Bottom panels:* logarithmic gray-scale image of 100 μm *IRAS* intensity. The logarithmic gray scale covers $-1.3 \leq I \leq 4.7$, with contours at $I = 10$, 100, and 1000 MJy sr^{-1}. The *IRAS* data were high-pass–filtered as described in § 5.1. *Middle Panels:* logarithmic gray-scale image of RFRR's 11 cm continuum "source component" $T_{B,s}$. The logarithmic gray scale covers $-2.2 \leq \log T_{B,s} \leq 2.2$, with contours at $T_{B,s} = 0.1$, 1, and 10 K. *Top Panels:* single-contour (0.2 K) map of RFRR's $T_{B,s}$. Numbers in the top panel indicate RRL velocities from Table 1. Areas covered by our cataloged worms (Table 2) are noted. The gray scales are logarithmic instead of linear, so as to deemphasize the high intensities at low $|b|$. This nonlinear compression makes the worms more easily discernible.

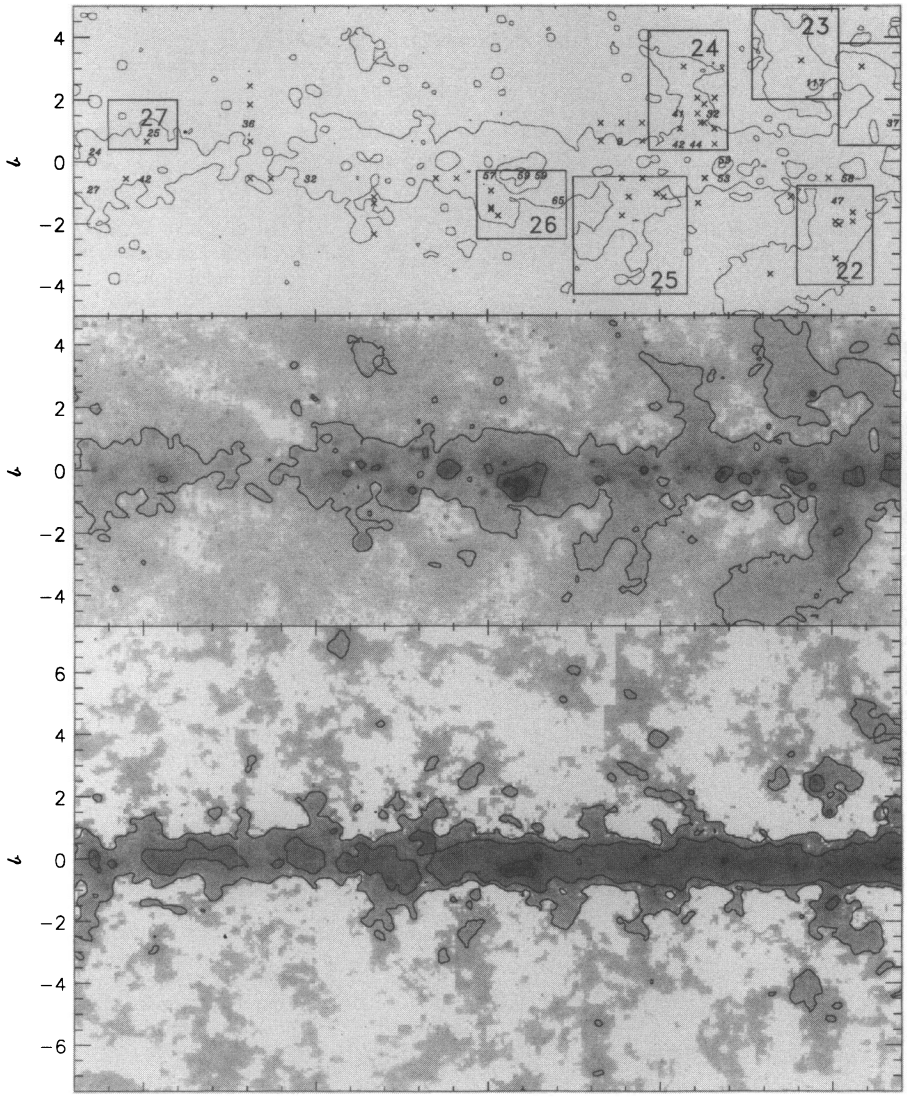

FIG. 7.—*Continued*

component data together with the *IRAS* 100 μm surface brightness. The *IRAS* map was spatially high-pass filtered (or "unsharp masked") by replacing each pixel with the difference between its original value and the median of a $3° \times 3°$ box centered on the pixel. The gray scales are logarithmic instead of linear so as to deemphasize the high intensities at low $|b|$, which makes the worms more easily discernible. For the middle plots of 11 cm continuum we provide contours at $T_{B,s} = 0.1$, 1, and 10 K, and for the bottom plots of *IRAS* 100 μm we provide contours at $I = 10$, 100, and 1000 MJy sr^{-1}. There is some correspondence between the radio and IR maps, although it is hardly perfect. But both maps show wispy structures that emulate the classical vertical structure of worms.

In the top panel of Figure 7, the velocity of each RRL detection is printed on top of a single-contour map of the RFRR source component. The boxes indicate areas covered by the worms cataloged in Table 2. We used the RFRR source component as a guide to select positions for our RRL observations. In most cases, we found that a single worm structure on Figure 7 had a characteristic RRL velocity. Thus, as seen in RRL emission, a worm is coherent in three dimensions. We used the detected RRL velocities, together with the morphology revealed in the RFRR source component map, to make a catalog of worms. Table 2 presents this list. Column (1) is a running number; column (2) is a name which is based on a rough estimate of the worm's central position in Galactic coordinates; column (3) is the area covered in square degrees; columns (4) and (5) are the LSR velocity and the velocity FWHM. Column (6) shows the number of positions in the worm that we observed, and column (7) the number of positions at which the RRL was detected; all of these positions are listed in Table 1. Column (8) gives associations with known H II regions and other comments.

Figure 8 displays the 21 cm line data from Weaver & Williams (1974), spatially high-pass filtered as was done for the *IRAS* data in Figure 7. The gray scale is "square root" as described in the figure caption. We show maps at specific velocities separated by 8.4 km s^{-1}; this is also the range covered by each map. These maps form a complete set of low-latitude H I maps for specific velocities, and are much

TABLE 2

OBSERVED PROPERTIES OF WORMS

Number (1)	Name (2)	Area (3)	V_{LSR} (4)	FWHM (5)	Number of Positions (6)	Number of Positions with Detections (7)	H I Association: Comment (8)
1	GW 0.0−1.4	3.6	7	35	2	2	KHR GW 0.5−5.9, $v = 9$, but not visible on Fig. 6
2	GW 3.7+1.5	5.8	14	32	9	5	No KHR association, but visible on Fig. 6 ($v = 16$); morphology allows classification as two separate worms, but because each one has the same velocity, we lump them together into one
3	GW 3.9−2.0	7.2	6	33	14	8	KHR GW 4.6−3.1, $v = 13$; Fig. 6 shows a nice circle
4	GW 6.3−1.5	12.2	6	28	10	7	KHR GW 6.5−3.7, $v = 22$
5	GW 7.7 + 1.6	8.7	18	25	7	7	
6	GW 9.6+1.0	1.9	21	39	4	4	
7	GW 10.7−3.0	13.0	21	36	26	18	
8	GW 12.2+1.3	12.6	28	37	17	17	KHR GW 12.3+1.8, $v = 25$, but not visible on Fig. 6
9	GW 13.5−1.3	2.8	27	36	7	7	
10	GW 16.2−2.0	11.5	28	32	27	25	KHR GW 14.9−1.6, $v = 31$; KHR GW 16.9−3.8, $v = 25$; Probably associated with worm 11
11	GW 18.5+2.8	31.7	26	27	60	55	KHR GW 17.8+3.0, $v = 28$; probably associated with worm 10
12	GW 19.0−1.5	6.6	51	40	18	17	KHR GW 19.5−6.4, $v = 32$
13	GW 23.6−1.8	3.6	77	33	15	11	KHR GW 23.0−1.6, $v = 78$:
14	GW 25.7+2.5	9.4	43	20	8	5	No KHR association, but visible on Fig. 6 ($v = 47$)
15	GW 28.6+3.0	5.3	2	25	4	2	
16	GW 26.9−2.5	17.6	...	...	11	0	
17	GW 29.5+2.3	5.5	90	49	11	7	Probably associated with worm 18
18	GW 30.5−2.5	17.1	93	43	32	30	KHR GW 31.6−5.9, $v = 78$: ; probably associated with worm 17
19	GW 35.1+1.2	2.2	75	40:	3	2	No KHR association, but possible H I structure on Fig. 6 ($v = 79$)
20	GW 35.1−1.4	7.7	57	30	20	16	KHR GW 35.8−2.2, $v = 44$
21	GW 38.0+1.6	10.5	42	20	8	5	KHR GW 39.7+5.7, $v = 30$
22	GW 39.8−2.1	7.3	52	36	8	2	KHR GW 40.0−5.5, $v = 33$:
23	GW 41.2+3.0	7.8	32	33	4	3	No KHR association, but possible H I structure on Fig. 6 ($v = 32$)
24	GW 44.0+1.9	9.5	41	36	18	6	KHR GW 46.4+5.5, $v = 32$, but not visible on Fig. 6; our V_{LSR} is questionable because all RRL data have marginal signal-to-noise
25	GW 45.9−2.3	13.4	...	...	8	0	
26	GW 49.1−1.4	6.2	60	28	16	12	KHR GW 47.9−1.8, $v = 67$; the KHR association is questionable, but the H I structure is visible on Fig. 6
27	GW 61.5+0.0	3.5	25	23	7	4	KHR GW 60.9+26, $v = 10$; worm goes both up and down

NOTE.—A number followed by a colon is uncertain.
Col. (1).—A running number.
Col. (2).—A name based on Galactic longitude and latitude.
Col. (3).—The approximate area occupied by the worm in square degrees.
Col. (4).—The average of RRL velocities for all positions within the worm.
Col. (5).—The average of the RRL FWHMs for all positions within the worm.
Col. (6).—The number of positions for the worm appearing in Table 1.
Col. (7).—The number of positions in the worm for which the RRL was detected.

more helpful than the maps presented by KHR, which were either a global H I map integrated over all velocities or just a few maps for specific velocities. Boxes on Figure 8 are the same boxes as in Figure 7, but only for worms whose velocities are known from the RRL data. In some cases, the KHR correspondences in Table 2 are easily visible on Figure 8, but in some cases they are not, and in some cases there are correspondences with H I features that are not listed by KHR. These discrepancies probably occur because KHR identified H I worms using the full velocity range instead of using specific velocities, and required correspondence with the diffuse *IRAS* emission; also, they used a computer algorithm to select worms.

In two regions, Table 2 lists worm pairs that are located at the same l but situated on opposite sides of the Galactic plane. The first example is worms 11 and 12 (GW 16.2−2.0 and GW 18.5+2.8), which have $V_{LSR} = 28$ and 26 km s^{-1}. Worm 12 may itself be an agglomeration: it includes the well-studied Stockert chimney (centered at $l \sim 18.^\circ5$) and possibly a weaker worm (centered at $l \sim 15.^\circ0$), both of which are clearly visible on Figure 1 of MRR; these authors allude to the possibility that these structures are associated. Worms 19 and 17 (GW 29.5+2.3 and GW 30.5−2.5) have $V_{LSR} = 93$ and 90 km s^{-1}. This pair is similar to the above pair in all respects except that neither member of this pair has been previously studied in detail.

If each of these two pairs is, in fact, a single object, then we have two huge structures that extend $\gtrsim 7^\circ$ and $\gtrsim 5^\circ$ in Galactic latitude. It is natural to reject the existence of such large structures simply because they *are* large. However, even larger structures are seen in the 21 cm line as supershells (Heiles 1979, 1984). Also Maciejewski et al. (1996) have found a new giant H I supershell, $\sim 7^\circ$ in diameter, which is associated with KHR's GW 35.8−2.2; it consists

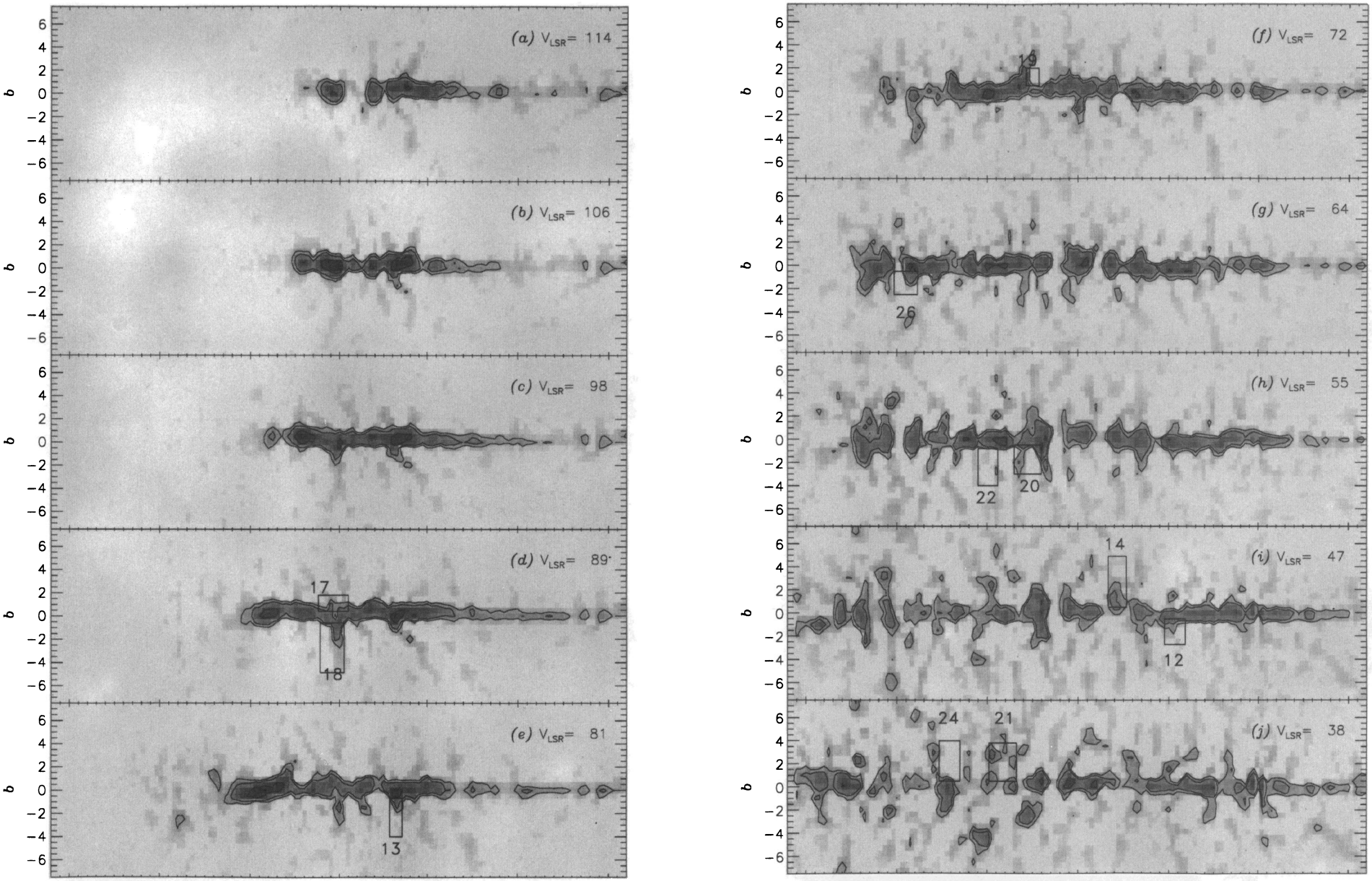

FIG. 8.—Twenty gray-scale maps of the 21 cm line intensity centered at specific velocities separated by 8.4 km s^{-1}; each map covers a range of 8.4 km s^{-1}. The horizontal scale is Galactic longitude, running from $l = 358°$ at the right to 62° at the left; major tick marks mark $l = 0°, 10°, \ldots, 60°$ (*right to left*). The intensities were high-pass–filtered identically to the *IRAS* data in Fig. 7, as described in § 5.1. The boxes represent all worms that are identified in the present paper (Table 2) and that have RRL detections so that the velocities are known; the boxes are the same as in Fig. 7. The gray scale is "square root," with white $\leq 1 \times 10^{20}$ and black $\geq 10 \times 10^{20}$ cm^{-2}. Contour levels are 1, 2, 5, and 10×10^{20} cm^{-2}.

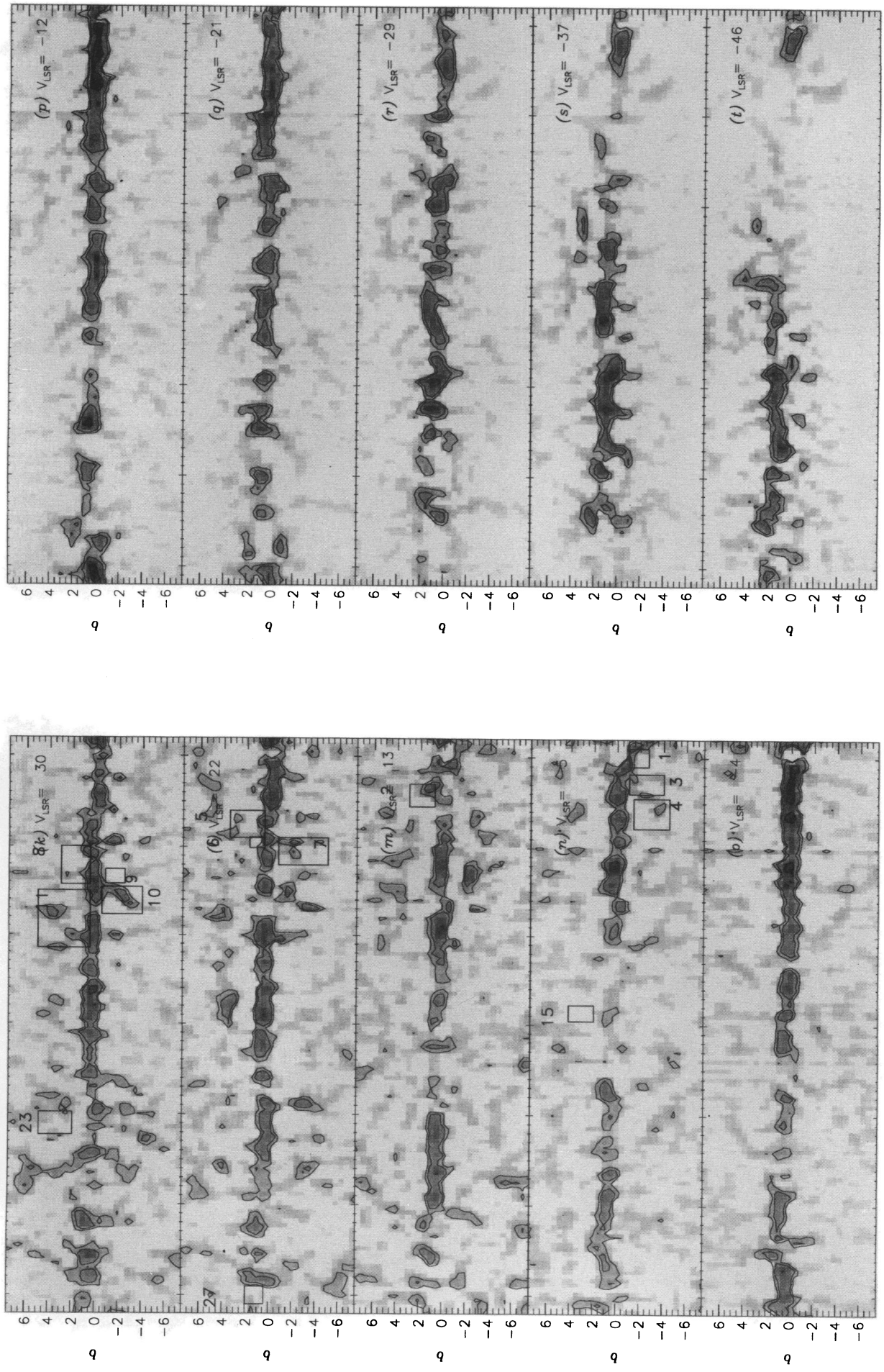

FIG. 8—*Continued*

of two negative-latitude worms, separated in l by $\sim 7°$, that are "capped" by very weak H I emission. We also note that, from the theoretical standpoint, worms are thought to be produced by clustered supernovae that blow holes in the Galactic gas layer, and when the supernovae are situated near $z = 0$ and there are enough of them, the resulting structure should extend both below and above $z = 0$. We cannot tell whether it is indeed correct to identify our two pairs as two single objects, but for the purposes of our catalog we opt for being conservative and retain the identification of them as two pairs.

Some of the worms in Table 2 are associated with H II regions, which lie near their bases at small $|b|$. To establish these associations, we used the early catalog of Reifenstein et al. (1970) because it contains only the stronger H II regions, which we thought would be more relevant for the association with worms. Also, Reifenstein et al. used somewhat coarse angular resolution and, as a result, sometimes lump several H II clumps together into one; this simplifies matters by reducing the number of H II regions associated with any particular worm. After making these associations, we consulted the more recent and complete catalog of DWBW and found associations with three additional worms. For many of these H II regions, DWBW have resolved the distance ambiguity associated with inner Galaxy objects by studying their H I and molecular absorption lines. We did not include Lockman's (1989) more extensive catalog for weaker H II regions because their distances are unknown.

Table 3 presents the associations of worms and H II regions, together with $R_{\rm Gal}$ and the two $d_\odot$ values calculated from $V_{\rm LSR}$ and l assuming the Galactic rotation law given by Burton (1988). For H II regions for which DWBW have resolved the distance ambiguity, we used our corresponding $d_\odot$. We determine $d_\odot$ for worms that were associated with H II regions by averaging our $d_\odot$ values of the associated H II regions.

There is one case where the distance ambiguity is not well resolved: the H II region complex W31, located near $l = 10°$ (Wilson 1974). The cold-gas absorption lines for W31 range up to $V_{\rm LSR} \sim 40$ km s^{-1}, and its RRL velocities are at ~ 10 km s^{-1}; the larger velocities for absorption lines imply that W31 is at the "far" distance, which is very large, ~ 15 kpc. However, even though the tangential velocity $V_{\rm max} \sim 200$ km s^{-1} in this direction, no absorption lines occur above ~ 40 km s^{-1}. It is highly unlikely that the long path length represented by this large velocity interval contains no cold gas. Wilson (1974) concludes that W31 is located in the "3 kpc arm" (see Roberts 1979 and Bania 1980), which lies ~ 5.1 kpc from the Sun; for the 3 kpc arm, the primary Doppler motion near $l = 10°$ is expansion instead of rotation. For our discussion, we assume that the distance to W31 is unknown.

5.2. *Sizes and Ionization Requirements*

Table 4 presents the sizes and ionization parameters for worms that have associated H II regions. Column (2) is the adopted distance $d_\odot$ in kiloparsecs from § 5.1; columns (3) and (4) show the rough extents parallel and perpendicular to the Galactic plane in parsecs, equal to Δl or Δb multiplied by $d_\odot$. Column (5) shows S_{49}, the UV photon luminosity required to keep the worm ionized in units of 10^{49} photons s^{-1} (calculated using Rubin 1968), and column (6) shows $S_{\rm worm}/S_{\rm tot}$, the ratio of the photon luminosity required for the worm to that for the worm plus the associated H II regions.

We explain in detail our technique for obtaining warm fluxes and areas. Deriving these quantities in an entirely objective way is impossible for two reasons: first, the definition of a worm is itself subjective; second, worms cover large angles and have low surface brightnesses, so a small change in the adopted zero point makes a large difference. Our procedure is as follows: (1) We examine the worm's box on Figure 7 and find the average brightness temperature $\langle T \rangle$ for all pixels having -0.07 K $< T_{B,s} < 0.6$ K. (2) We find the number of pixels having $T_{B,s} > 0.02$ K, which gives the area as listed in Table 2; (3) we multiply $\langle T \rangle$ by the area and convert to janskys. This technique makes the resulting flux less sensitive to the exact location of the worm's box, particularly to its lower $|b|$ edge. The upper cutoff in $T_{B,s}$ eliminates the contribution from bright H II regions.

A few entries in Table 4 require some explanation. Worms GW 0.0−1.4, GW 10.7−3.0, and GW 12.2+1.3 have associated H II regions, but the $d_\odot$ values for these regions are not known; thus we can provide only the S_{49} ratios, which are independent of distance. GW 29.5+2.3 appears even though it has no associated H II region; we have assumed its distance is the same as that of GW 30.5−2.5, with which it is associated in position and velocity.

Sizes are typically several hundred parsecs. The median S_{49} is about 15. The average S_{49} is 36, with a dispersion of 38. These statistics mean that the distribution of S_{49} is asymmetric, having a long "tail" for large values. A single O5 star produces $S_{49} \sim 4.7$ (Osterbrock 1989). Thus the ionization of the median worm requires a large star cluster, about 3 times larger than that which produces the Orion Nebula plus its associated Orion/Eridanus worm (see below). Such star clusters are common in the Galaxy and produce the bright H II regions that are easily observed at radio wavelengths.

The five most powerful worms in Table 4 require $S_{49} > 55$, while the remainder (except for one) have $S_{49} < 20$; this is a big gap and may be physically meaningful. For convenience in the later discussion, we define worms having $S_{49} > 55$ as "giant" worms. The required values of S_{49} scale as $d_\odot^2$, so it is not surprising that all of the giant worms lie at the "far" distance. Are these distances reliable? For three of these (including the two strongest), namely, GW 3.7+1.5, GW 25.7+2.5, and GW 38.0+1.6, the "near" and "far" distances differ by large factors, about 3.0 for the first and 3.9 for the two strongest, and if they instead lie at the "near" distances, then their required S_{49} ratios would lie comfortably in the range of those of the other worms. Such errors in distance might occur if our identification of the associated H II regions is incorrect.

For the other two, GW 29.5+2.3 and GW 30.5−2.5, the situation may be more compelling. First, these two worms may themselves be associated, because they lie on opposite sides of the Galactic plane and have the same $V_{\rm LSR}$; if so, then their combined requirement is $S_{49} = 136$. Although this is enormous, it is comparable to the requirement of the associated H II regions, which makes it reasonable because it means that the ionizing photons are roughly equally divided. Furthermore, the "near" and "far" distances of these worms differ by a factor of only ~ 1.8; even if the worms lie at the "near" distance, their combined requirement is $S_{49} = 42$, which is still very high. However, it is very

TABLE 3

DERIVED PROPERTIES OF WORMS

Number/Name (1)	V_{LSR} (2)	FWHM (3)	S(Jy) (4)	R_{Gal} (5)	d_1 (6)	d_2 (7)	$d_\odot$ (8)	S_{49} (9)
1/GW 0.0−1.4 (C1)	7	35	20.5	...	...	...	...	...
G359.73−0.41	12.0	23.0	2.4	...	...	...	...	...
G0.56−0.85	15.0	20.0	3.5	...	...	...	...	...
2/GW 3.7+1.5	14	32	39.5	4.2	12.7	4.3	13.8	73.2
G4.4+0.1	9.1	17.6	6.2	5.5	14.0	3.0	14.0	11.5
G3.3−0.1	4.0	36.7	2.2	6.1	14.6	2.4	14.6	4.1
3/GW 3.9−2.0	6	33	55.0	6.1	14.5	2.4	...	...
4/GW 6.3−1.5	6	28	150.1	6.8	15.2	1.7	1.3	2.5
G6.0−1.2 (M8)	3.0	13.5	85.1	7.6	16.0	0.9	0.9	1.4
5/GW 7.7+1.6	18	25	103.0	5.3	13.6	3.3	3.3	10.9
G8.1+0.2	19.3	20.5	5.8	5.2	13.5	3.3	3.3	0.6
6/GW 9.6+1.0	21	39	17.7	5.4	13.6	3.2	...	...
7/GW 10.7−3.0 (C2)	21	36	135.5	5.6	13.7	3.0	...	...
G10.2−0.3 (W31)	13.9	20.6	51.8	6.3	14.5	2.3	...	...
G10.3−0.1 (W31)	9.7	15.6	13.6	6.9	15.1	1.7	...	...
G10.6−0.4 (W31)	0.3	14.8	10.2	8.5	16.7	0.0	...	...
8/GW 12.2+1.3	28	37	109.0	5.3	13.3	3.3	...	...
G11.90+0.75	25.5	24.0	2.3	5.4	13.5	3.2	...	...
9/GW 13.5−1.3	27	36	23.9	5.6	13.5	3.1	3.5	2.9
G12.8−0.2 (S41/W33)	36.3	18.3	44.9	4.8	12.7	3.8	3.8	5.3
G14.6+0.1 (S41/W33)	37.2	13.2	24.3	5.1	12.8	3.6	3.6	2.9
10/GW 16.2−2.0	28	32	122.2	5.8	13.5	2.8	2.4	6.9
G15.1−0.7 (M17/S45/W38)	17.2	24.8	534	6.6	14.4	2.0	2.0	29.9
11/GW 18.5+2.8	26	27	287.5	6.2	13.7	2.5	2.6	18.9
G17.0+0.8 (M16/S49/W37)	24.5	18.0	107.8	6.2	13.8	2.5	2.5	7.1
G18.5+1.9 (W35/S54)	32.9	18.7	102.6	5.8	13.2	2.9	2.9	6.7
12/GW 19.0−1.5 (C3)	51	40	63.2	4.9	12.1	3.9	4.0	9.8
G19.1−0.3 (W39)	67.8	13.3	17.0	4.3	11.4	4.7	4.7	2.6
G19.7−0.2	43.4	22.4	12.4	5.3	12.5	3.5	3.5	1.9
G20.7−0.1	57.4	16.7	14.5	4.9	11.8	4.1	11.8	...
13/GW 23.6−1.8	77	33	37.7	4.5	10.7	4.8	10.3	38.9
G22.8−0.3 (W41)	82.5	32.2	45.5	4.3	10.6	5.1	10.6	46.9
G23.4−0.2	101.5	13.5	13.2	3.9	9.7	5.9	9.7	13.6
14/GW 25.7+2.5 (C4)	43	20	80.7	5.9	12.2	3.1	12.0	113.0
G25.29+0.31	45.0	25.0	0.9	5.8	12.1	3.2	...	...
G25.70+0.03	52.0	22.0	2.2	5.5	11.7	3.6	11.7	3.1
15/GW 28.6+3.0	2	25	37.5	8.5	0.0	14.9	...	...
16/GW 26.9−2.5	...	...	135.7	...	...	...	...	...
17/GW 29.5+2.3 (C5)	90	49	77.6	4.6	9.4	5.5	8.8	58.4
18/GW 30.5−2.5 (C5)	93	43	126.3	4.6	8.8	5.8	8.8	95.1
G28.6+0.0	96.2	13.3	14.4	4.4	9.1	5.8	9.1	10.8
G29.9−0.0	96.4	15.7	21.1	4.5	8.8	5.9	8.8	15.9
G30.2−0.2	101.8	10.5	9.2	4.4	8.3	6.4	8.3	6.9
G30.8−0.0 (W43)	92.3	20.2	97.4	4.6	8.9	5.7	5.7 (KB)	73.4
G31.1+0.0	99.2	9.1	8.0	4.5	8.3	6.3	8.3 (KB)	6.0
19/GW 35.1+1.2	75	40:	20.6	5.3	9.1	4.9	...	...
20/GW 35.1−1.4	57	30	69.9	5.9	10.2	3.7	3.4	7.9
G34.3+0.1 (W44)	53.9	10.6	15.0	5.9	10.5	3.5	3.5	1.7
G35.2−1.7 (W48)	46.7	18.7	15.3	6.2	10.8	3.1	3.1	1.7
21/GW 38.0 + 1.6	42	20	103.5	6.5	10.6	2.8	9.9	98.7
G37.6−0.1	55.8	16.5	7.9	6.0	9.8	3.7	9.8	7.5
G37.9−0.4 (W47)	60.2	16.0	24.4	5.9	9.4	4.0	9.4	23.3
22/GW 39.8−2.1	52	36	93.1	6.2	9.6	3.5	...	...
23/GW 41.2 + 3.0	32	33	60.0	7.0	10.6	2.2	...	...
24/GW 44.0+1.9	41	36	76.2	6.7	9.4	2.9	...	...
25/GW 45.9−2.3	...	...	93.3	...	...	...	...	...
26/GW 49.1−1.4	60	28	61.6	6.4	5.6	5.6	5.0	15.0
G49.0−0.3 (W51)	63.2	10.8	111.3	6.4	5.6	5.6	5.6	27.1
G49.2−0.3 (W51)	67.2	19.4	12.0	6.4	5.6	5.6	5.6	2.9
G49.5−0.4 (W51)	58.2	18.8	117.4	6.5	5.5	5.5	5.5	28.5
G51.2−0.1	55.3	23.7	37.0	6.6	5.3	5.3	5.3	9.0
27/GW 60.5+0.0	25	23	24.2	7.6	5.9	2.4	...	...

unlikely that they lie at the "near" distance because the resolution of the distance ambiguity is consistent for all five H II regions.

Table 4 lists one worm for which the primary data do not come from Table 1. This is the Orion/Eridanus worm. The Eridanus loop is visible in H I (Heiles 1976) and Hα emission (Reynolds & Ogden 1979, hereafter RO) and is associated with the Orion A and Orion B H II regions. RO find $S_{49,\mathrm{worm}} \sim 3.9$; for the H II regions, we obtain $S_{49} = 1.0$ from the flux densities of Mezger & Henderson (1967). Table 4 shows that the Orion worm is comparable in its total ionization requirement to other Galactic worms. However, it has much smaller EM than the worms in Table 4. RO's Figure 7 shows that, outside of Barnard's loop, the peak EM is about 100 cm^{-6} pc. Such small EMs are undetectable in RRLs. As compared to worms in the Galactic interior, the Orion/Eridanus worm has a larger area and a lower surface brightness.

TABLE 4

ADDITIONAL DERIVED PROPERTIES OF WORMS HAVING ASSOCIATED H II REGIONS

Number/Name (1)	$d_\odot$ (2)	ΔR (3)	Δz (4)	S_{49} (5)	$S_{\mathrm{worm}}/S_{\mathrm{tot}}$ (6)
1/GW 0.0−1.4.....	...	...	...	...	0.78
2/GW 3.7+1.5.....	13.8	720	600	73.2	0.82
4/GW 6.3−1.5.....	1.3	40	90	2.5	0.64
5/GW 7.7+1.6.....	3.3	100	100	10.9	0.95
7/GW 10.7−3.0	...	...	...	...	0.64
8/GW 12.2+1.3	...	...	...	...	0.98
9/GW 13.5−1.3	3.5	60	60	2.9	0.26
10/GW 16.2−2.0	2.4	130	80	6.9	0.19
11/GW 18.5+2.8	2.6	250	180	18.9	0.58
12/GW 19.0−1.5	4.0	140	80	9.8	0.68
13/GW 23.6−1.8	10.3	220	200	38.9	0.39
14/GW 25.7+2.5	12.0	360	650	113.0	0.96
17/GW 29.5+2.3 (C1).....	8.8	380	520	58.4	0.19
18/GW 30.5−2.5 (C1).....	8.8	610	250	95.1	0.31
20/GW 35.1−1.4	3.4	110	70	7.9	0.70
21/GW 38.0+1.6	9.9	350	310	98.7	0.76
26/GW 49.1−1.4	5.0	330	110	15.0	0.18
28/Orion/Eridanus	0.5	250	330	3.9	0.80

NOTE.—"C" in col. (1) followed by a number means the worm has a comment

Col. (1).—The number and name of the worm.

Col. (2).—The adopted distance in kiloparsecs from Table 3.

Col. (3).—The rough horizontal extent of the worm in parsecs.

Col. (4).—The rough vertical extent of the worm in parsecs.

Col. (5).—S_{49}, the luminosity of ionizing photons required to produce the ionization, from Table 3.

Col. (6).—The ratio of photon luminosity for the worm to that for the worm plus all associated H II regions.

COMMENTS ON INDIVIDUAL WORMS.—(C1) For GW 29.5+2.3 and GW 30.5−2.5, the ratios in col. (6) are equal to the flux of each worm divided by the flux of both worms plus all of their associated H II regions, because we believe that the two worms are associated.

The Stockert chimney, which forms part of GW 18.5+2.8, is the most well-studied worm (MRR), but in terms of size and ionization requirements it is mediocre. GW 29.5+2.3 and GW 30.5−2.5—and especially their combination, which is probably real—are the largest and most energetic worms in our sample. They are associated with the W43 complex of H II regions. W43 is indeed a giant H II region: it is the fourth largest on the list of DWBW. W43 has been studied in detail by Lester et al. (1985).

6. OBSERVATIONAL AND THEORETICAL PERSPECTIVE

6.1. *Observations Support the "Worm"/"Chimney" Paradigm*

An operative scenario for worms and chimneys has been put forth by several authors and now exists as a standard paradigm (Norman & Ikeuchi 1989; Heiles 1990). With respect to thermal radio continuum and RRL emission, the paradigm invokes clusters of massive stars together with successive generations of star formation: supernovae in the older generations of a star cluster blow a huge supershell or "worm," the interior of which contains the hot ionized medium (HIM), and hot stars in successive generations of the same cluster produce ionizing photons that can travel freely to the distant worm walls, which become fully ionized with low emission measures (the "worm-ionized medium" or W-IM; Heiles 1992, 1993a, b).

There is an important distinction between the terms "worm" and "chimney" (Heiles 1992). Large cavities tend to be extended in the z-direction, which is what led to their original definition as "worms" (Heiles 1984). If the cavity becomes open at the top and vents to the gaseous halo, then it is a "chimney" (Norman & Ikeuchi 1989). In practice it is currently impossible to determine whether any structure is indeed open at the top. Until this observational fact has

FOOTNOTES TO TABLE 3

NOTE.—Entries are grouped for each worm. The first line in each group is the worm; the succeeding lines are associated H II regions. "C" in col. (1) followed by a number means the worm has a comment.

Col. (1).—The number and name of the worm or the name of the H II region.

Cols. (2) and (3).—V_{LSR} and FWHM (km s^{-1}). For worms these are from Table 1. For H II regions they are from Reifenstein et al. 1970. H II regions with positions given to one decimal place are from Reifenstein et al.; those with two decimal places are from Downes et al. 1980.

Col. (4).—The flux density in janskys.

Col. (5).—The Galactocentric radius in kiloparsecs (see text, § 5.1).

Cols. (6) and (7).—The near and far distances from the Sun in kiloparsecs (see text, § 5.1).

Col. (8).—$d_\odot$, the adopted distance from the Sun (see text, § 5.1). The choice between near and far distances is from Downes et al. 1980, unless followed by "(KB)" when it is from Kuchar & Bania 1994. For worms the adopted distance is the mean of the "near" or "far" distance of the associated H II regions and the worm itself. For the H II regions distances used for calculating S_{49} are the adopted distance for the worm, not the individual distances to the H II regions, because they are all assumed to be associated.

Col. (9).—S_{49}, the luminosity of ionizing photons required to produce the ionization (see text, §§ 5.1 and 5.2).

COMMENTS ON INDIVIDUAL WORMS.—(C1) We do not assign a distance to GW 0.0−1.4 because, at $l = 0°$, kinematic distances are impossible to obtain. (C2) We do not assign a distance to either GW 10.7−3.0 or its associated H II regions (including W31); see text, § 5.1. (C3) In GW 19.0−1.5, the H II region G20.7−0.1 is at the far distance, while the other H II regions associated with worm GW 19.0−1.5 are at the near distance; we assume that GW 19.0–1.5 is at the near distance and that G20.7−0.1 is not associated with the worm. The leaders in the S_{49} column for G20.7−0.1 means that it is assumed to be not associated with the worm and the other H II regions in the group. (C4) GW 25.7+2.5 has such a large S_{49} (and flux) compared to its associated H II region that we are probably making an incorrect association. (C5) We assume that GW 29.5+2.3 and GW 30.5−2.5 are associated, so that the H II regions listed are associated with both.

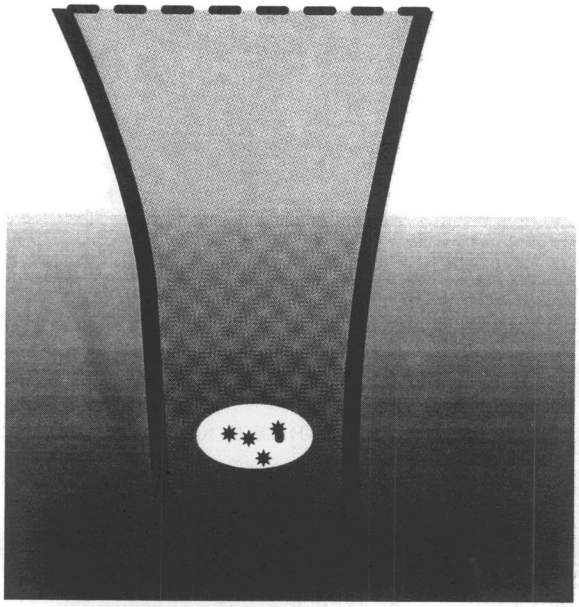

FIG. 9a

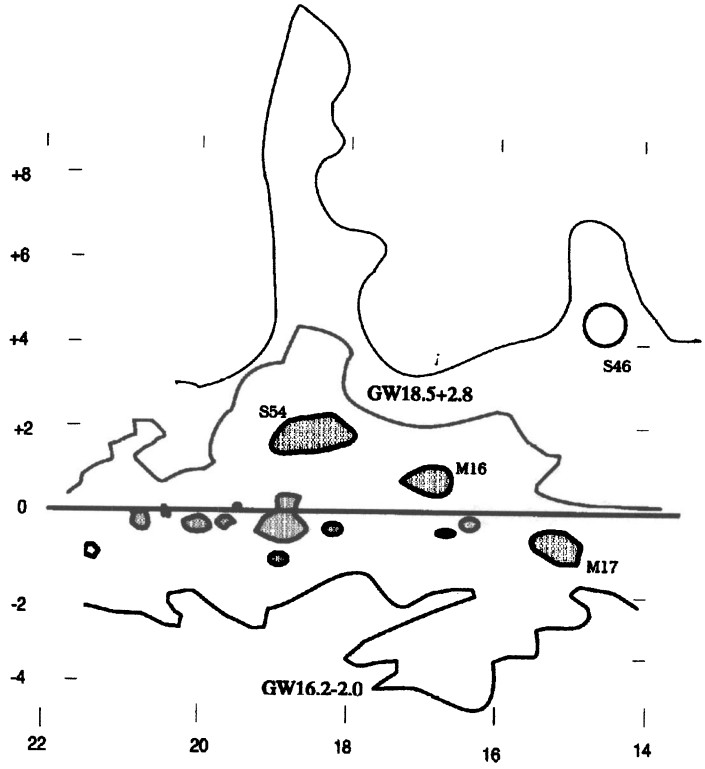

FIG. 9b

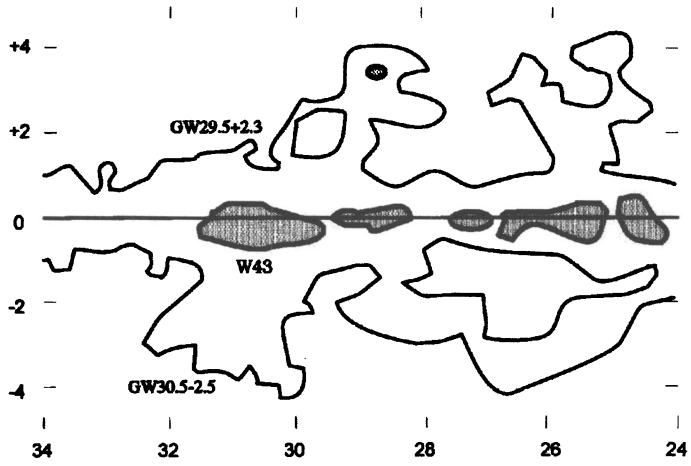

FIG. 9c

FIG. 9.—(*a*) Sketch of the "textbook example" of a chimney. A chimney is a special case of a worm, being open at the top and connecting to the gaseous Galactic halo; a worm is not necessarily open. Ideally, older generations of massive stars in the star cluster exploded as supernovae, creating the large cavity which contains the hot ionized medium (HIM); hot stars in the current generation of the same cluster produce ionizing photons that can travel freely to the distant worm walls, which become fully ionized with low emission measures (the "worm-ionized medium" or W-IM). In this sketch, the white ellipse represents the molecular cloud out of which new generations of stars will form; massive stars tend to form at the edge of a molecular cloud. (*b*) Worm GW 18.5+2.8, which consists of the Stockert chimney (protuberance at $l \sim 18°.5$) and a weaker protuberance at $l \sim 15°$. The upper thin contour is the 0.15 K contour from the 2720 MHz Stockert telescope data (MRR's Fig. 1a), and the other two contours are the 0.1 and 1 K contours from RFRR's 2695 MHz "source component." The three strong H II regions are denoted by the most common designations and have the following correspondences: (S54, W35); (M16, S49, W37); (M17, S45, W38). With M16 at the base of the worm, centered between the two protuberances, this corresponds roughly to the textbook example. (*c*) Worms GW 29.5+2.3 and GW 30.5−2.5, together with six nearby H II regions that have closely similar V_{LSR}. The two contours are the 0.1 and 1 K contours from RFRR's 2695 MHz "source component." The W43 is the fourth most powerful in DWBW's list of Galactic H II regions. The hatched areas show where RRLs having $V_{LSR} \sim 95$ km s^{-1} exist; it is possible that all of these areas belong to one giant structure. It is very likely that GW 29.5+2.3 and GW 30.5−2.5 are really the same structure, produced by the group of H II regions at their base; this would correspond reasonably well with the textbook example of (*a*).

been determined, it is more correct to call an object a "worm" instead of a "chimney."

Morphologically, the "textbook chimney" should look like Figure 9*a*, which is an idealization in several respects. First, with its perfectly cylindrically symmetric shape, it implicitly assumes a preexisting uniformly distributed interstellar medium (ISM) in both horizontal and vertical directions. Second, it envisions that nothing but HIM fills the

cylinder volume; however, moderately dense "interstellar clouds" should be swept up by the shock and will occupy the volume, although they will suffer evaporation and should eventually dissipate. Third, there may be more than one star cluster and H II region involved in the worm's production and ionization.

The textbook example has the H II region centered at the base of the worm and centered with respect to the cylindrical walls. The structure should be "edge-brightened" because it is hollow. We compare this idealized picture with the nearest worm and the two largest worms.

The Orion/Eridanus region is the nearest and most easily observed example, and it also offers excellent support for the paradigm. The expansion of the Eridanus loop is evident in both the 21 cm and Hα lines. The loop contains the HIM at $T \sim 2 \times 10^6$ K and is prominent in soft X-ray emission (Burrows et al. 1993). The Orion region has undergone several generations of star formation (Blaauw 1964). The classic model of the Orion region has the hot, massive stars just outside the molecular cloud, so that the H II region is density-bounded on the side away from $b = 0°$ and ionization-bounded toward $b = 0°$, where the molecular cloud resides; see the excellent review by Goudis (1982, chap. 1), the large-scale Hα photograph by Sivan (1974), and the definitive discussion by RO. The Orion/Eridanus worm differs from those in the Galactic interior in its larger size and smaller surface brightness; this is probably a result of a lower ISM pressure in the solar vicinity as compared to the more supernova-dominated Galactic interior, which is predicted by models of supernova-dominated ISM (McKee & Ostriker 1978).

For GW 18.5+2.8 (which includes the Stockert chimney), Kundt & Müller (1987, hereafter KM) provide a convenient sketch that shows just the essentials; we show the equivalent in Figure 9*b*. The Stockert chimney per se is the long, thin protuberance centered at $l \sim 18\overset{\circ}{.}5$ that extends up to $b \sim 8°$ on Figure 9*b*. The large H II region S54 (W35) lies at the base of this worm. If this is the worm structure in its entirety, then it may depart from the textbook example because there is no obvious brightening. However, in § 5.1 above we listed GW 18.5+2.8 as being much larger because RRL emission at $V_{LSR} \sim 26$ km s^{-1} covers $15° \lesssim l \lesssim 21°$. Although the H II region S54 is not centered at the base of this composite worm, the similarly powerful H II region M16 is. We conclude that the combined structure is the relevant one and that the previous studies, which concentrated only on the portion called the Stockert chimney, underemphasized the horizontal size scale by a factor of ~5. In § 5.1 above we also argued that this composite worm may be associated with its negative-*b* counterpart, GW 16.2−2.0; if so, then the total conglomerate is very large.

With this expanded interpretation the combined structure is very large, with an angular extent in $l \gtrsim 5°$. With the distance of 2.5 kpc, this makes the linear extent ≳220 pc, and with the *b* height ≳8° for the Stockert chimney portion it extends to at least $z = 350$ pc. One aspect of GW 18.5+2.8 that departs from the worm/chimney paradigm is the presence of H II regions at the bases of *both* protuberances; the paradigm would have H II regions located only near the middle. This may mean that the protuberances are not the worm walls but are somehow associated with the presence of dense ISM near the H II regions.

The combination of GW 29.5+2.3 and GW 30.5−2.5 (the "W43 worm") is by far the largest worm structure in our sample, if it is indeed real. Figure 9*c* presents a very rough sketch of GW 29.5+2.3 and GW 30.5−2.5, again showing just the essentials. There are two vertical protuberances, one at positive *b* centered at $l \sim 30°$ and one at negative *b* centered at $l = 31°$. A third positive-*b* protuberance, centered at $l \sim 25.5°$, has a different V_{LSR} except in portions of its base ($b \lesssim 1°$). At negative latitudes lies a structure that is better described as a "large, diffuse blob" than as a "protuberance," centered near $l \sim 26\overset{\circ}{.}5$ with $\Delta b \sim 5°$; we were unable to detect RRLs from the blob, which is not surprising because it is so dim, but we did find some negative-*b* RRLs near $l \sim 25°$, $b \gtrsim -1°$. The two well-defined protuberances near $l \sim 30°$, the base of the positive-*b* protuberance near $l \sim 26\overset{\circ}{.}5$, and a negative-*b* region near $l \sim 25°$ all have roughly the same V_{LSR}. This, together with the string of six H II regions within $25\overset{\circ}{.}5 \lesssim l \lesssim 31\overset{\circ}{.}5$ that also have the same V_{LSR}, suggests that all of these objects may be part of one giant structure. If so, it would be far the largest in our sample: the angular extent is $\Delta l \sim 6°$ and $d_\odot \sim 8.8$ kpc, providing a linear diameter ~900 pc and a vertical extent (*top to bottom*) ≳8° or ≳1200 pc (we use lower limits on the vertical extent because the apparent angular extent is probably limited by sensitivity). This huge structure is not particularly well described by the "textbook example," but with six separate star clusters contributing to its energization and ionization, this is not surprising.

High-$|z|$ CO appears to be associated with at least two worms. Weak CO emission at high $|z|$ seems to exist generally in the inner Galaxy, according to preliminary results from a survey by Dame & Thaddeus (1994, 1995). These results happen to include $|b|$ scans lying on the two worms GW 30.5−2.5 (the "W43 worm") and GW 49.1−1.4 (the "W51 worm"), where there appears to be excess emission associated with the worms. For the W43 worm, the RRL velocity range is 75–110 km s^{-1} and the CO velocity range is 60–100 km s^{-1}. For the W51 worm, the RRL velocity range is 55–67 km s^{-1} and the CO velocity range is 35–60 km s^{-1}. The RRL and CO velocity ranges coincide fairly well for both worms. We believe that the association of RRL and CO emission is real, but a more complete mapping of the high-*z* CO emission is required to solidify the association by comparing morphologies; we eagerly anticipate additional results from this important CO survey. To pursue the association further, we estimate the mass of the molecular gas by scaling the velocity and area-integrated CO brightness temperature (from Figs. 3 and 5*a* of Dame & Thaddeus 1995) by the factor $N(H_2)/W(CO) = 2.3 \times 10^{20}$ cm^{-2} K^{-1} km^{-1} s (Strong et al. 1988) and using the distances derived from Galactic rotation (Table 4). For the W43 worm, the inferred mass of molecular gas is $\sim 2 \times 10^5$ $M_\odot$. For comparison, the estimated mass of atomic gas, derived from Figure 8, is 4 times larger, $\sim 8 \times 10^5$ $M_\odot$. Thus the molecular gas, if indeed associated with the worms, is a nontrivial fraction of the total mass. The energy required to levitate the molecular gas to its observed $|z|$-height is not large ($\sim 10^{51}$ ergs), but it is noteworthy because either this energy must be imparted to the molecular gas without dissociating the molecules or the molecules must be formed in the worm walls.

Finally, consider the vertical surface brightness structure of these worms in terms of a simple model consisting of a cylindrical cavity of radius R_2 (the subscript 2 means units of 100 pc) with a cluster of stars at its center that produces

an ionizing photon flux S_{49}. Suppose that the photons travel in straight lines to the cylinder walls, where they ionize the gas. Then the emission measure EM perpendicular to the cylinder wall as a function of height z above the cluster is

$$\mathrm{EM}_\perp = 10.0 S_{49}\, T_4^{0.7} R_2^{-2} \left(1 + \frac{z^2}{R^2}\right)^{-3/2} . \qquad (9)$$

Figures 10*a* and 10*b* present eyeball fits of this function to restricted observations in these two worms in the form $\mathrm{EM} = \mathscr{C}\{1 + [(b - b_0)^2/\Delta b^2]\}^{-3/2}$. For GW 18.5+2.8 (the S54 worm), the observational data are the 17 continuum brightness temperatures from Table 4 of MRR, which sample only the brighter parts of the Stockert chimney (we exclude their point for the H II region S54). For GW 30.5−2.5 (the W43 worm), the observational data are the averages of our RRL integrated intensities over $29.^\circ5 \le l \le 32^\circ$, for b at half-degree intervals. The parameters of the fits displayed in the figures are $(\mathscr{C}, b_0, \Delta b) = (21{,}000, 1.^\circ87, 0.^\circ375)$, (9000, 0.°0, 0.°93) for the Stockert chimney and GW 30.5−2.5, respectively; the offsets b_0 are roughly where the associated H II regions S54 and W43 are centered. The fits are quite good and suggest that the model is a reasonable description of the data.

For each worm in our sample we have included mainly just the region of l where the worm is bright. For the expanded interpretation in which the bright portions are the tangentially seen walls of a much larger structure, this means that the observed EM is larger than the $\mathrm{EM}_\perp$ represented in equation (9). In more representative parts of the large worms the wall is not seen tangentially, and $\mathrm{EM}_\perp$ by itself is too small to produce observable radio continuum or RRL emission. A correct and detailed interpretation of the vertical structure would require additional observations that would sample the full extent of these combined structures with very high sensitivity and a theoretical model that better represents the shape of the structures. This is beyond the scope of the present paper.

6.2. *Ionization State of Worms and Their* H II *Regions*

Concerning the association of worms with H II regions, the W-IM paradigm must allow for three empirical classes of worm.

Class 1.—The worm is visible in H I but is not visible, or is weak, in thermal radio emission. Of the candidate worms listed by KHR, which were selected using H I data alone, some are real; the real ones that do not appear in thermal radio emission belong to class 1. For these worms, which formed from earlier generations of stars, there are two possibilities: (1) The current generation of stars is surrounded by sufficient amounts of molecular gas to prevent any ionizing photons from leaving, so that all ionizing photons are trapped in clouds near the stars and produce classical ionization-bounded H II regions. (2) Star formation has ceased, so that no hot stars currently exist to produce ionizing photons. In the first case, a class 1 worm will have one or more classical H II regions at its base.

Class 2.—The worm is visible in H I and exhibits strong thermal radio emission. For these worms, enough of the dense molecular clouds has been eroded away by ionization and blown away by supernovae from previous generations of stars that there now exist clear paths for ionizing photons to reach the distant worm walls. Observations show that many young stars form near the edge of a molecular cloud instead of inside the cloud; this is crucial in allowing the existence of class 2 worms. One expects the H II region to be density-bounded on the side away from the Galactic plane, where the ISM volume density is smallest and where explosions more easily create large cavities; however, this may not always be the case because the ISM is inhomogeneous. In some cases, the newly formed massive stars lie close to or inside the molecular cloud where they were born, and we expect at least half the photons to ionize the molecular cloud, creating a standard H II region that is ionization bounded on at least one side. If the stars remain close to their parent molecular cloud, then the ratio $S_{\mathrm{worm}}/S_{\mathrm{tot}} \lesssim 0.5$. However, this need not be the case. For example, if the hot stars lie far enough from the parent cloud, then the cloud will intercept few ionizing photons and the resulting H II region will be weak. As we discuss below, the Orion/Eridanus worm illustrates the latter case, in which $S_{\mathrm{worm}}/S_{\mathrm{tot}} > 0.5$. This can also happen when most of the molecular cloud has been dispersed. Thus, in reality, the ratio could achieve any value.

Class 3.—The worm is visible in H I, but the radio continuum is dominated by nonthermal (synchrotron) radi-

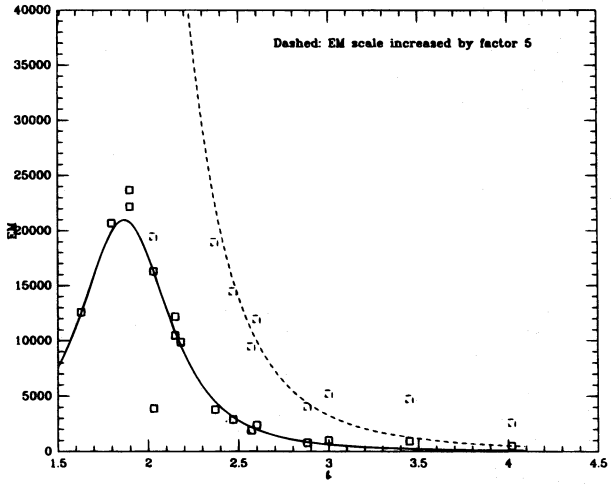

FIG. 10*a*

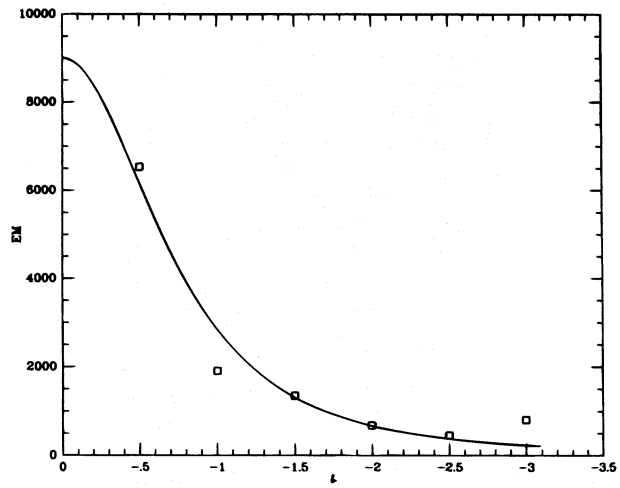

FIG. 10*b*

FIG. 10.—(*a*) Squares show the observed EM vs. b in the Stockert chimney (units for EM: cm^{-6} pc). The line is an eyeball fit of eq. (9). The dashed squares and line are the same quantities, with the vertical scale exaggerated by a factor of 5. (*b*) Squares show the observed EM vs. b for GW 30.5−2.5 (units for EM: cm^{-6} pc). The line is an eyeball fit of eq. (9).

ation; thermal radio radiation may or may not be present. Many worms exhibit some nonthermal continuum: we recall Figure 3, where the spread of points to the right of the left-hand envelope is almost certainly a result of nonthermal radiation (§ 3). Some worms are almost exclusively nonthermal emitters, as the nearby large shell, the North Polar Spur (Radio Loop I), shows. Two synchrotron-dominated worms probably exist in Table 2: for GW 26.9−2.5 and GW 45.9−2.3, we did not detect RRLs. Given the energetic nature of worm formation, the production of relativistic electrons is no surprise.

Our data fit reasonably well into these classes. First, Table 2 associates 16 worms with H I features, with fairly high (but not full) confidence; some of these associations are made using KHR's list, and some using the maps in Figure 8. The total number of worms in Table 2 with which it would be possible to associate H I on the basis of RRL velocities is 25; thus 64% of the worms have an associated H I feature. To achieve perfect consistency with our classification scheme, this fraction should be 100%. The absence of perfect consistency probably results from difficulty in making an H I identification because of confusion in the H I angular structure. However, it would also occur if some of our worm identifications in Table 2 are incorrect or if the worm/chimney paradigm is not the only one that is relevant for these structures. We adopt the viewpoint that a 64% association rate is acceptable because of confusion in the H I structure and that the first explanation given above is correct.

Second, Table 3 shows that 17 of the 25 worms that have RRL emission, or 68%, are associated with H II regions. The remaining 32% have no associated H II regions, and in the above scenario are in their final phase of class 2 when the molecular cloud has been totally disrupted. This is probably consistent with expectation: as reviewed by Heiles (1990), ionizing photons persist for ~20 Myr, and star formation persists for ~15 Myr, so that molecular clouds (and thus classical H II regions) should exist in ~75% of the cases. However, statistics derived from Table 3 are very uncertain and possibly incorrect because our sample is not unbiased. In the present paper, we have selected our observed points on the basis of the large-scale Galactic 11 cm continuum emission. This allows us first to find worms and then to determine whether they are associated with H II regions. The reverse procedure would search for worms associated with H II regions. We cannot predict the biases that might be associated with our selection technique.

Table 4 shows that six of the 18 worms (33%) have $S_{worm}/S_{tot} \leq 0.5$. (These ratios are very uncertain, as explained in § 5.2; thus, this statistic is very uncertain.) We interpret these low ratios as characterizing worms in which the hot stars all reside close to the parent molecular cloud. It is conceivable, but hardly necessary, that this implies that star formation has been occurring for a relatively short time and that these worms are relatively young.

The Orion/Eridanus worm is a well-observed case, and shows conclusively that the ratio S_{worm}/S_{tot} is not a good indicator of whether the molecular cloud has been disrupted. Table 4 shows that $S_{worm}/S_{tot} \sim 0.80$. However, the Orion region still produces stars at a rapid rate and has a large reservoir of molecular gas. The large value of S_{worm}/S_{tot} is caused by stars in the I Ori association that have moved away from the parent molecular cloud (RO).

Finally, we note that in RRL emission the worms show only H^+ and no He^+ (HKLR). Thus, the photons that escape to the worm walls must have a soft spectrum, with few photons above 24.6 eV. It is not obvious how this might happen. We suggest that in class 2 worms the hottest stars might be preferentially located within the dense molecular cloud, which could trap the He-ionizing photons. This is sensible because the hottest stars have the shortest lifetimes and therefore the least opportunity to escape their parent clouds. Alternatively, in some worms the last generations of star formation might have an IMF that systematically excludes the more massive stars. Investigation of these suggestions requires further study.

6.3. *The Absence of Worm Structures for Two Powerful H II Regions*

W51 and W43 are the second and fourth most powerful H II regions on DWBW's list, and have associated worms on our list. In contrast, the first and third most powerful H II regions on DWBW's list, G25.382−0.177 (V_{LSR} = 59 km s^{-1}) and G43.169+0.002 (W49; V_{LSR} = 10 km s^{-1}), do not. Even though the latter two are about twice as far away as W43, their worm structures could not go unnoticed if the structures were comparable in size to that of W43. In the worm picture, these regions have just begun to form massive stars.

6.4. *Completeness of Our Sample: Total Galactic Population*

Figure 6*a* shows the location of worms with well-determined distances in a face-on view of the Galaxy, together with the TC spiral arms, derived from the information in Table 4. The worms are very well confined to the spiral arms. This is only somewhat surprising, because these worms are all associated with relatively strong H II regions that have well-determined distances, and these H II regions themselves were used to define the spiral arms by Georgelin & Georgelin (1976). However, it is not a tautology—except in the sense of our worm/chimney scenario—because from the purely empirical standpoint we have no a priori reason to expect worms to be associated with strong H II regions.

More important from the standpoint of discussing the completeness of the sample, most (12 of 15) of the worms lie in the Galactocentric azimuth range $90° < \theta < 180°$. If the number of worms in each Galactocentric quadrant is the same, which should be roughly correct even in the absence of axisymmetry, then the total number of worms that we would detect in a complete survey is about 48. We note, however, that even for the most easily observed Galactocentric quadrant $90° < \theta < 180°$, our survey is almost certainly incomplete: the density of worms decreases with distance from the Sun. Therefore, the estimate of 48 worms is almost certainly too low, but probably not by more than a factor of 2 or so.

We also have five giant worms (§ 5.2) in Table 4. The total ionization requirement for these five giant worms is $S_{49} \sim 420$, for an average of 84 each. It is easier to see giant worms, so our listing of them should be more complete than for smaller worms. It seems reasonable to suppose that these five represent a third of the total number of giant worms in the Galaxy.

Summing up, a fairly complete sample of worms in the Galaxy would contain $\gtrsim$50 ordinary worms (a lower limit

because of incompleteness) and about 15 giant worms. From Table 4, the average for ordinary nongiant worms is $S_{49} \sim 12$. Thus, the total Galaxy-wide ionization requirement for all inner Galaxy worms is $S_{49} \gtrsim 1900$. HKLR review the total Galactic ionization requirement for the ELDWIM alone and obtain $S_{49} \sim 1.1 \times 10^4$. We conclude that globally the worms require only a small fraction ($\sim$17%) of the photons that ionize the ELDWIM. This is commensurate with Mezger's (1978) classic discussion of the ELDWIM, which considered its scale height to be $\sim$85 pc, much smaller than the typical height of a worm.

7. SUMMARY

We have searched for 1.4 GHz radio recombination lines at 583 positions, mostly toward the Galactic interior, and achieved detections at 418 positions. These data characterize the extended low-density electron component (the ELDWIM).

1. We derive an electron temperature of 7000 K from a comparison of RRL and radio continuum intensities, using equation (1) and the eyeball fit to the left-hand envelope of points on Figure 4*b*. We estimate that RRL intensities are increased over their LTE values by $f_{\rm NLTE} \sim 1.3$. There exist real variations in temperature, in particular toward lower values, but the fraction of gas with much lower temperatures is small.

2. We examine the distribution of the ELDWIM with the velocity-longitude diagram of Figure 5*c*. This exhibits some concentration into spiral arms, but seemingly less than that of strong H II regions (Fig. 5*a*). The distribution of the ELDWIM seems similar to that of weak H II regions (Fig. 5*d*), but a definitive conclusion regarding physical association awaits a detailed statistical study. The distribution of the ELDWIM is not too dissimilar from that of CO. Figure 5*c* bears no resemblance to Figure 5*b*, which shows a simulated distribution of points to represent the azimuthally symmetric inner Galaxy ring component of Taylor & Cordes (1993). We argue that their ring component does not exist, and we propose a small modification in their spiral arm model (§ 4.3 and Fig. 6); we concentrate the ELDWIM in these arms By comparing the thermal radio continuum and the pulsar dispersion measures over long path lengths, we derive the ELDWIM filling factor in the spiral arms to be $\phi_{\rm WIM} \sim 0.01$ and the electron density in the emitting regions ~ 5 cm^{-3}. Figure 5*d* directly compares the ELDWIM RRLs with H II regions for $l < 60°$ and shows that the ELDWIM does not necessarily reside near an H II region.

3. Figure 7 presents spatially high-pass–filtered, compressed gray-scale images of the diffuse radio continuum and 100 μm IR emission, together with the RRL velocities. These diffuse emissions are characterized by vertical structures that correspond well to the "worm" and "chimney" models, in which clustered supernovae blow large cavities in the gaseous disk that may connect to the gaseous halo. Some of the RRL emission (our very crude estimate is $\sim$17%) lies in vertical structures. We interpret the RRL emission from these structures in terms of the "worm-ionized medium," in which the thermal radio emission arises in the worm walls; the walls are ionized by photons from hot stars in the cluster whose supernovae originally produced the cavity. The nearest example is the Orion/Eridanus cavity. The previously best-studied example is the Stockert chimney, which we argue is part of a much larger structure. We discuss ionization requirements for the worms and their associated H II regions and define three classes that describe the ionization of worm walls. These classes depend on the state of star formation in the central molecular cloud, which eventually dissipates. High-$|z|$ CO may be associated with at least two large worms.

4. Figure 6*a* shows that the worms for which distances can be reliably determined are closely confined to spiral arms. In § 6.4 we discuss the global ionization requirement for all worm walls and find that it is small (our very rough estimate is $\sim$17%) compared to the total requirement for the Galactic ELDWIM.

Note added in manuscript.—Normandeau, Taylor, and Dewdney (1996) have used the Synthesis Telescope at the Dominion Radio Astrophysical Observatory to map the 21 cm line at high resolution and to discover a large, nearly textbook-perfect chimney in the outer Galaxy. It is a prominent cavity seen in H I, it has the bright H II region W4 at its base, and its walls are ionized by the stars in W4. This observation shows that spectacular worms, and also supershells (Heiles 1979, 1984), can exist in the outer Galaxy. However, the total number of such objects in the outer Galaxy should be small, reflecting the relatively small star formation rate in the outer Galaxy.

The HCRO RRL observations were one of the last major projects to be undertaken with the now defunct 85 foot telescope. We take particular pleasure in thanking Harold Weaver, the founder of HCRO, for his pioneering efforts in building both the observatory, which still exists, and the telescope, which remained productive for 31 years. This work was supported in part by an NSF grant to C. H. B.-C. K. has been supported in part by the 1994 KOSEF International Cooperative Research Fund.

REFERENCES

Anantharamaiah, K. R. 1985, J. Astrophys. Astron., 6, 177, 203
———. 1986, J. Astrophys. Astron., 7, 131
Bahcall, J. N., Schmidt, M., & Soneira, R. M. 1983, ApJ, 265, 730
Bania, T. M. 1980, ApJ, 242, 95
Blaauw, A. 1964, ARA&A, 2, 213
Burrows, D. N., Singh, K. P., Nousek, J. A., Garmire, G. P., & Good, J. 1993, ApJ, 406, 97
Burton, W. B. 1988, in Galactic and Extragalactic Radio Astronomy, ed. G. L. Verschuur & K. I. Kellermann (2d ed.; Berlin: Springer), 295
Cersosimo, J. C. 1990a, ApJ, 349, 67
———. 1990b, in Radio Recombination Lines: 25 Years of Investigation, ed. M. A. Gordon & R. L. Sorochenko (Dordrecht: Kluwer), 237
Cersosimo, J. C., Azcárate, I. N., Hart, L., & Colomb, F. R. 1989, A&A, 208, 239
Clifton, T. R., & Lyne, A. G. 1986, Nature, 320, 43
Combes, F. 1991, ARA&A, 29, 195
Cooper, B. F. C. 1976, in Methods of Experimental Physics, 12B, 280
Cordes, J. M., Weisberg, J. M., Frail, D. A., Spangler, S. R., & Ryan, M. 1991, Nature, 354, 121
Dame, T. M., & Thaddeus, P. 1994, ApJ, 436, L173
———. 1995, in The Physics of the Interstellar and Intergalactic Medium, ed. A. Ferrara, C. F. McKee, C. Heiles, & P. R. Shapiro (San Francisco: ASP), 15
Dickey, J. M., & Lockman, F. J. 1990, ARA&A, 28, 215
Downes, D., Wilson, T. L., Bieging, J., & Wink, J. 1980, A&AS, 40, 379 (DWBW)
Frail, D. A., & Weisberg, J. M. 1990, AJ, 100, 743
Georgelin, Y. M., & Georgelin, Y. P. 1976, A&A, 49, 57
Goudis, C. 1982, The Orion Complex: A Case Study of Interstellar Matter (Dordrecht: Reidel)

Heiles, C. 1976, ApJ, 208, L137
———. 1979, ApJ, 229, 533
———. 1984, ApJS, 55, 585
———. 1989, ApJ, 336, 808
———. 1990, ApJ, 354, 483
———. 1992, in Evolution of Interstellar Matter and Dynamics of Galaxies, ed. J. Palouš, W. B. Burton, & P. O. Lindblad (Cambridge: Cambridge Univ. Press), 12
Heiles, C. 1993a, in Reviews in Modern Astronomy 6: Stellar Evolution and Interstellar Matter, ed. G. Klare (Hamburg: Astron. Gesellschaft), 19
———. 1993b, in Star Formation, Galaxies and the Interstellar Medium, ed. J. Franco, F. Ferrini, & G. Tenorio-Tagle (Cambridge: Cambridge Univ. Press), 245
———. 1994, ApJ, 436, 720
Heiles, C., Koo, B-C., Levenson, N. R., & Reach, W. R. 1995, ApJ, 462, 326 (HKLR; Paper I).
Johnston, S., Lyne, A. G., Manchester, R. N., Kniffen, D. A., D'Amico, N., Lim, J., & Ashworth, M. 1992, MNRAS, 255, 401
Jonas, J. L., de Jager, G., & Baart, E. E. 1985, A&AS, 62, 105
Koo, B-C., Heiles, C., & Reach, W. T. 1992, ApJ, 390, 108 (KHR)
Kuchar, T. A., & Bonia, T. M. 1994, ApJ, 436, 117
Kulkarni, S. R., & Heiles, C. 1987, in Interstellar Processes, ed. D. J. Hollenbach & H. A. Thronson, Jr. (Dordrecht: Reidel), 87
Kundt, W., & Müller, P. 1987, Ap&SS, 136, 281 (KM)
Lester, D. F., Dinerstein, H. L., Werner, M. W., Harvey, P. J., Evans, N. J., & Brown, R. L. 1985, ApJ, 296, 565
Lockman, F. J. 1976, ApJ, 209, 429
———. 1979, ApJ, 232, 761
———. 1980, in Radio Recombination Lines, ed. P. A. Shaver (Dordrecht: Reidel), 185
———. 1989, ApJS, 71, 469
Maciejewski, W., Murphy, E. M., Lockman, F. J., & Savage, B. D. 1996, ApJ, in press
McKee, C. F., & Ostriker, J. P. 1978, ApJ, 218, 148
Mezger, P. G. 1978, A&A, 70, 565
Mezger, P. G., & Henderson, A. P. 1967, ApJ, 147, 471
Müller, P., Reif, K., & Reich, W. 1987, A&A, 183, 327 (MRR)
Norman, C. A., & Ikeuchi, S. 1989, ApJ, 345, 372
Normandeau, M., Taylor, A. R., & Dewdney, P. E. 1996, Nature, 380, 687
Osterbrock, D. E. 1989, Astrophysics of Gaseous Nebulae and Active Galactic Nuclei (Mill Valley: University Science Books)
Petuchowski, S. J., & Bennett, C. L. 1993, ApJ, 405, 591
Press, W. H., Flannery, B. P., Teulolsky, S. A., & Vetterling, W. T. 1989, Numerical Recipes (Cambridge: Cambridge Univ. Press), 86
Reach, W. T., Heiles, C., & Koo, B.-C. 1993, in Back to the Galaxy, ed. S. Holt & F. Verter (New York: AIP), 548
Reich, W., Fürst, E., Reich, P., & Reif, K. 1990, A&AS, 85, 633 (RFRR)
Reifenstein, E. C., Wilson, T. L., Burke, B. F., Mezger, P. G., & Altenhoff, W. J. 1970, A&A, 4, 357
Reynolds, R. J. 1991, ApJ, 372, L17
Reynolds, R. J., & Ogden, P. M. 1979, ApJ, 229, 942 (RO)
Roberts, W. W. 1979, in IAU Symp. 84, The Large-Scale Characteristics of the Galaxy, ed. W. B. Burton (Dordrecht: Reidel), 175
Rubin, R. 1968, ApJ, 154, 391
Sharpless, S. 1959, ApJS, 4, 257
Shaver, P. A., McGee, R. X., Newton, L. M., Danks, A. C., & Pottasch, S. R. 1983, MNRAS, 204, 53
Sivan, J. P. 1974, A&AS, 16, 163
Strong, A. W., et al. 1988, A&A, 207, 1
Taylor, J. H., & Cordes, J. M. 1993, ApJ, 411, 674, (TC)
Weaver, H., & Williams, D. R. W. 1974, A&AS, 17, 1
Williams, D. R. W. 1973, A&AS, 8, 505
Wilson, T. L. 1974, A&A, 31, 83